# The Conformational Landscape of the Ribosomal Protein S15 and Its Influence on the Protein Interaction with 16S RNA

Thomas Créty and Thérèse E. Malliavin
Laboratoire de Biochimie Théorique, CNRS UPR 9080, Institut de Biologie Physico-Chimique, 75 005 Paris, France

ABSTRACT The interaction between the ribosomal protein S15 and its binding sites in the 16S RNA was examined from two points of view. First, the isolated protein S15 was studied by comparing NMR conformer sets, available in the PDB and recalculated using the CNS-ARIA protocol. Molecular dynamics (MD) trajectories were then recorded starting from a conformer of each set. The recalculation of the S15 NMR structure, as well as the recording of MD trajectories, reveals that several orientations of the N-terminal $\alpha$-helix $\alpha1$ with respect to the structure core are populated. MD trajectories of the complex between the ribosomal protein S15 and RNA were also recorded in the presence and absence of $Mg^{2+}$ ions. The $Mg^{2+}$ ions are hexacoordinated by water and RNA oxygens. The coordination spheres mainly interact with the RNA phosphodiester backbone, reducing the RNA mobility and inducing electrostatic screening. When the $Mg^{2+}$ ions are removed, the internal mobility of the RNA and of the protein increases at the interaction interface close to the RNA G-U/G-C motif as a result of a gap between the phosphate groups in the UUCG capping tetraloop and of the disruption of S15-RNA hydrogen bonds in that region. On the other hand, several S15-RNA hydrogen bonds are reinforced, and water bridges appear between the three-way junction region and S15. The network of hydrogen bonds observed in the loop between $\alpha1$ and $\alpha2$ is consequently reorganized. In the absence of $Mg^{2+}$, this network has the same pattern as the network observed in the isolated protein, where the helix $\alpha1$ is mobile with respect to the protein core. The presence of $Mg^{2+}$ ions may thus play a role in stabilizing the orientation of the helix $\alpha1$ of S15.

## INTRODUCTION

During the formation of the ribosome 30S subunit, the protein S15 is among the first proteins, along with S18, S6, and S11, interacting with the 30S central domain (1). S15 binds to a phylogenetically conserved three-way junction formed by the intersection of helices H20, H21, and H22 of eubacterial 16S RNA (Fig. 1). The free 16S RNA undergoes an equilibrium (2) between an unfolded conformation, in which the junction is planar with $\sim$120° interhelical angles, and a folded conformation, in which two helices, H21 and H22, become collinear and the third, helix H20, forms a 60° angle with respect to H22. From the observations made in the literature, it was concluded (2) that the $Mg^{2+}$ ions as well as the protein stabilize the RNA folded conformation.

The ribosomal protein S15 from *Thermus thermophillus* was cocrystallized with a 57-nucleotide 16S rRNA fragment containing shortened helices H20, H21, and H22 (3). The two helices H21 and H22 are capped by UUCG tetraloops, which are called TL1 and TL2 in the following (4). The 2.8 Å resolution of the crystal structure of the complex (Protein Data Bank (PDB) id: 1dk1, Fig. 2 *a*) shows (3) that S15 interacts in the minor groove with the three-way junction (first binding site) and a G-U/G-C motif (second binding site). The protein structure consists of four $\alpha$-helices, the helices $\alpha1$ (residues 3–15), $\alpha2$ (residues 24–45), $\alpha3$ (residues 49–73), and $\alpha4$ (residues 73–81). The S15 structure in the complex is similar to the structure of the free protein previously determined by NMR (PDB id: 1ab3, Fig. 2 *b*) (5). Nevertheless, in the crystallographic structure of the free S15 protein from *Bacillus stearothermophilus* (PDB id: 1a32, Fig. 2 *c*) (6), the N-terminal helix $\alpha1$ protrudes from the body of the molecule to make contacts with a neighboring protein in the crystal lattice.

Nine $Mg^{2+}$ ions were positioned in the S15 RNA complex structure according to the observation of strong peaks of electronic density (3), and three of them are supposed to contribute to the junction stability. The $Mg^{2+}$ ions were previously shown in the literature to play an important role in the mechanism of ribozyme catalysis (7,8), in the folding of RNA (9–13), in the stability of the ribosome (14), and in the interaction between RNA and proteins (15,16) and ligands (17). Molecular dynamics (MD) simulations were performed to study the influence of $Mg^{2+}$ ions on the conformation of an RNA kissing loop (18), on the conformation of the 5S rRNA loop E motif (19), and on the conformation of the RNA-protein complex between *E. coli* loop E/helix IV rRNA and L25 protein (20).

The $Mg^{2+}$ ions are supposed to stabilize the folded form of the RNA three-way junction and thus to enhance the S15 binding (2) by increasing the bimolecular association rate. However, the effect of the $Mg^{2+}$ ions on the protein-RNA interaction at the atomic level has not yet been investigated. We analyze here MD simulations of the S15-RNA complex in the absence and in the presence of $Mg^{2+}$ ions to study the influence of $Mg^{2+}$ on the protein-RNA interaction. MD trajectories of the protein S15 are also analyzed to explore the

*Submitted July 4, 2006, and accepted for publication December 13, 2006.*

Address reprint requests to Thérèse E. Malliavin, Laboratoire de Biochimie Théorique, CNRS UPR 9080, Institut de Biologie Physico-Chimique, 13 rue P. et M. Curie, 75 005 Paris, France. Tel.: 33-1-58-41-51-68; Fax: 33-1-58-41-50-26; E-mail: therese.malliavin@ibpc.fr.



0006-3495/07/04/2647/19 $2.00

doi: 10.1529/biophysj.106.092601

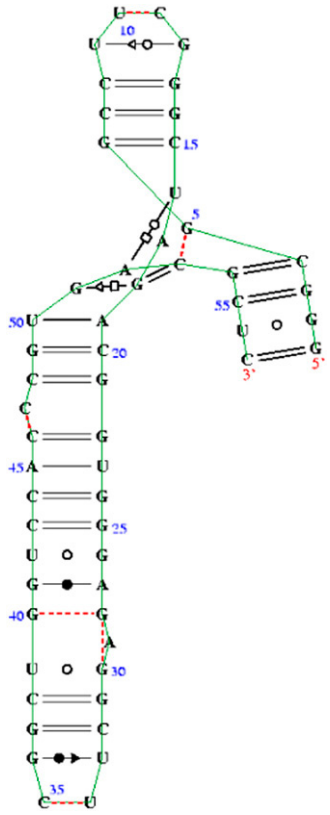

FIGURE 1 Secondary structure of the three-way junction RNA involved in the interaction with S15. The basepairing is displayed according to the ontology developed by Leontis and Westhof (59). The basepair between G51 and C53 was not displayed to improve the figure readability. This figure was realized with S2S (60).

conformational landscape of the free protein and relate it to the protein behavior in the complex. As said previously, the interaction of S15 with 16S RNA is one of the first steps in the 30S subunit formation, and a detailed inspection of the

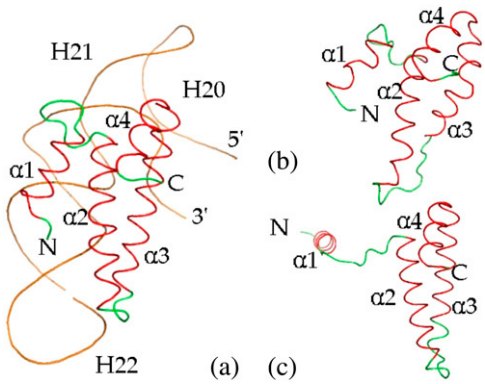


FIGURE 2 Structures of the S15-RNA complex (x-ray (1dk1) (*a*)), and of S15 (NMR (1ab3) (*b*)), and x-ray (1a32) (*c*)). The structures are shown in cartoon; the RNA is brown, and S15 is green and red in the $\alpha$-helices. The N- and C-terminal parts of the protein are shown as well as the 5′ and 3′ ends of RNA. The $\alpha$-helices S15 and the helices H20, H21, and H22 of RNA are also shown in the figure. This figure was realized with PyMOL 0.98 (61).

S15-RNA interaction features may thus be important for targeting the ribosome formation (21). Indeed, S15 was detected in a crystal structure of the 70S ribosome (22) in a bridge spanning the ribosomal subunit interface and seems to be essential for an efficient formation of the ribosome from the 30S and 50S subunits (23).

The use of MD simulations has proved to be a valuable tool for analyzing the behavior of systems including RNA (see McDowell et al. (24) and references cited therein). Nevertheless, the electrostatics of the $Mg^{2+}$ ions is modeled here using a single point charge without including the polarizability. This approximation is certainly crude but cannot be avoided because introduction of polarizability (25) would result in an excessive computational load for a several-nanosecond trajectory. Another limitation of the MD simulations of nucleic acids is the difficulty of modeling the conformation of the phosphodiester backbone (26). But, there is not much drift of the phosphodiester backbone angles from the crystallographic structure during the time interval studied in the work presented here.

## MATERIALS AND METHODS

The starting point of the MD trajectories recorded on the protein S15 was the first conformer of the PDB NMR structure (5) of S15 (PDB id: 1ab3) and the smallest-energy conformer of the NMR structure recalculated in the work presented here using the CNS-ARIA protocol. The starting conformation for the simulations of the S15-RNA complex was the x-ray crystallographic structure (3) of the S15-RNA complex (PDB id: 1dk1). Two molecular conformations are present for residues 27–29 of RNA in the 1dk1 file: the conformation A corresponding to the maximum number of formed basepairs was selected.

The parm98 parameter set (27) and the TIP3P model for water (28) were used in simulations. The motion equations were integrated with versions 6 and 7 of the program AMBER (29), respectively, for the isolated protein and for the complex. The cutoff of the Lennard-Jones interaction was 9 Å, and the long-range electrostatic interactions were calculated using the Particle Mesh Ewald protocol (30). The Lennard-Jones parameters of the $Mg^{2+}$ ions were taken from Aqvist (31) and correspond to an integration radius of 0.7926 Å and a well depth of 0.8947 kcal/mol. Trajectories of 15 ns were recorded for each studied system: the 1ab3 NMR conformer of S15, the 2fkx conformer of S15 calculated in the work presented here, and the x-ray structure of the S15-RNA complex in the presence and the absence of $Mg^{2+}$ ions, with a temperature of 298 K and a pressure of 1 atm. The atom coordinates were saved each 1 ps.

In case of the simulation of S15-RNA in the presence of $Mg^{2+}$ ions, the solute includes the nine crystallographic $Mg^{2+}$ ions but not the three $Na^+$ and $K^+$ ions observed in the crystal. The counterions were added in the vicinity of the charged groups of the solute using a Coulombic potential on a grid, using the command AddIons of leap. The charge of the isolated protein was neutralized with chloride ions, whereas sodium ions were added to neutralize the complex S15-RNA. For the simulation in absence of $Mg^{2+}$ ions, the $Na^+$ ions were not placed at the positions of removed $Mg^{2+}$. The resulting modeling is thus related to the presence or absence of a counterion, more than the electronic properties (polarizability) of the ions. This counterbalances the limitations of the treatment of electrostatics in the system and the uncertainty of the determination of the ion types in crystallographic structures.

The concentration of $Mg^{2+}$ ions is ~40 mM, which is a value of the same order as the experimental concentration used to study the S15-RNA interaction (2). On the other hand, the concentrations of $Na^+$ ions in the S15-RNA simulations are ~140 mM in the presence of $Mg^{2+}$ ions and ~220 mM in absence of these ions. The removal of the $Mg^{2+}$ ions thus introduces only a

small perturbation of the electrostatic field around the complex, and the effect produced by their disappearance is not produced by a nonspecific electrostatic effect.

The solute conformations were hydrated by a box of water molecules in a pseudoequilibrated configuration. The water molecules farther than 9 Å from any solute molecule were discarded. The simulation parameters (box dimensions, numbers of water molecules and atoms, type and number of counterions) are given in Table 1, along with a name for each trajectory.

Heating and system equilibration were performed as follows: 10 ps of heating up to 298 K at constant volume was done while solute atom locations were restrained with a harmonic restraint of 25 kcal/mol Å$^2$, followed by 5 ps of MD at constant volume and four MD rounds of 2.5 ps at constant pressure. The restraints on the solute atoms were progressively reduced to zero during these six rounds. No restraint was applied on the positions of $Mg^{2+}$, $Na^+$, or $Cl^-$. The isothermal-isobaric unrestrained simulations were performed using the Berendsen algorithm (32) for temperature bath coupling. The equations of motion were integrated using a time step of 2 fs. All covalent bonds involving hydrogen atoms were kept rigid using SHAKE (33).

The analysis was mainly performed with the program ptraj (29). The analysis of the conformational drift during the trajectories of the s15-rna complex and the monitoring of the S15, RNA, and complex electrostatic energies (data not shown) show that the s15-rna trajectories are stabilized in the 11–15-ns interval. The comparison of the s15-rna-mg and s15-rna trajectories was then based on mean and standard deviation values calculated on this interval. On the other hand, the trajectories s15-pdb and s15-aria were included integrally into the analysis, as the purpose of their analysis was to compare the conformational drift and the conformational landscapes of the structures 1ab3 and 2fkx.

During the simulation of the complex, the protein residues are numbered from 1 to 86 (corresponding to residues 101–186 of the 1dk1 file), the RNA residues are numbered from 87 to 143 (corresponding to residues 1–57 of the 1dk1 file), and the $Mg^{2+}$ ions are numbered from 144 up to 152 (corresponding to residues 200–206 and 208–209 of the 1dk1 file). The residue numbers given in the analysis are those used in the MD simulation; the corresponding numbers of the 16S RNA, if they exist, are underlined in parentheses.

The calculation of S15 conformers under NMR restraints was performed using the simulated annealing protocol available in the CNS-ARIA protocol (34), which was recently used for the recalculation of NMR structures in the RECOORD database (35). The scripts were downloaded from http://www.ebi.ac.uk/msd-srv/docs/NMR/recoord/scripts.html. The nonbonded force field was PROLSQ, and the covalent geometry was parallhdg5.3.pro (36). The conformers of the NMR structure and the conformations of S15 observed in the trajectories were thus obtained in the presence of two different force fields, which alleviates the possible bias induced by the use of a unique force field.

The NMR restraints were 965 nuclear Overhauser effect (NOE) distance restraints and 38 dihedral restraints provided by H. Berglund and already applied in Berglund et al. (5). These restraints were supplemented by adding 76 hydrogen bond restraints ($i$, $i + 4$) between amide hydrogens and carboxyl oxygens in $\alpha$-helices. The definition of the $\alpha$-helices was taken from the header of the 1ab3 file. The 25 best-energy conformers were selected from the 100 conformers calculated using the CNS-ARIA protocol. Among them, conformers displaying outlier orientations of the helices $\alpha$1 and $\alpha$4 were removed. The set of S15 conformers and the restraints used are deposited at the Protein Data Bank (id: 2fkx).

The NMR structures were analyzed using PROCHECK v.3.5.4 (37) and WHATIF 8.1 (38). The root mean-square deviation (RMSD) values between the conformer coordinates were calculated on the backbone atoms. The NOE distance restraints were examined in the NMR structures and in the trajectories by calculating, for each restraint, all distances $r_i$ separating the hydrogen pairs involved in the NOE. The mean distance value $R$ was then determined as

$$R^{-6} = \langle r_i^{-6} \rangle_i, \quad (1)$$

the mean value $\langle\rangle_i$ being calculated on the hydrogen pairs and on the trajectory snapshots or on the NMR conformers. The NOE restraint is violated for values of $R$ larger than $L + 1$ Å, where $L$ is the restraint upper bound. Each dihedral restraint was evaluated by calculating the mean dihedral angles along the trajectory and is violated if the mean value is located outside the restraint interval.

The variation of S15 tertiary structure was monitored by calculating the angles and the distances between the helix axes. The points belonging to each helix axis were determined as the middles of the backbone atom segments (N($i$), N($i$+2)), (C$\alpha$($i$), C$\alpha$($i$+2)), and (C′($i$), C′($i$+2)), where the residue numbers $i$ vary along the secondary structure element. The angle between two axes was defined as the angle between the vectors linking the first and the last point of each axis. The distance between two helix axes was calculated as the minimum distance between the points defining the axes.

## RESULTS AND DISCUSSION

### Analysis of the S15 NMR structures

The comparison of 2fkx and 1ab3 conformers (Fig. 3) shows a large increase in 2fkx of the mean percentage of residues located in the core Ramachandran regions determined by PROCHECK (Table 2, part a). Similarly, the percentages of residues in the allowed and in the generously allowed regions decrease. Thus, the 2fkx conformers display better Ramachandran parameters than the 1ab3 conformers. The mean number of bad contacts observed by PROCHECK is also considerably reduced if the conformers are calculated with the CNS-ARIA scripts.

The WHATIF $Z$-scores (Table 2, part b) show a picture similar to the PROCHECK analysis. The mean $Z$-score values are improved, and all $Z$-scores are in the −4/4 range for the 2fkx conformers. The number of bumps detected by WHATIF is also much reduced in the 2fkx conformers. The improved quality of 2fkx comes from the optimization of the conformers in the torsion angle space (39,40) as well as from the use of a final refinement step in water (41).

The number of violated nuclear Overhauser effect (NOE) restraints is divided by two in the 2fkx conformers with respect to the 1ab3 conformers (Table 2, part c): this decrease comes from a much smaller number of long-range violations as well as a smaller number of ($i$, $i + 1$) violations (Table 3). Nevertheless, the number of violated dihedral restraints slightly increases in 2fkx (Table 2, part c).

**TABLE 1 MD simulations run on the S15 isolated molecule, and on the S15-RNA complex**

| Simulation name | Solute | Number of water molecules | Number of atoms | Box size (Å, Å, Å) | Duration (ns) | Ions |
|---|---|---|---|---|---|---|
| s15-pdb | S15 (1ab3) | 6,130 | 19,905 | 73, 66, 55 | 15 | 8 $Cl^-$ |
| s15-aria | S15 (2fkx) | 6,405 | 20,730 | 75, 67, 53 | 15 | 8 $Cl^-$ |
| s15-rna-mg | S15-RNA (1dk1) | 11,219 | 37,018 | 79, 67, 69 | 15 | 9 $Mg^{2+}$, 31 $Na^+$ |
| s15-rna | S15-RNA (1dk1) | 11,018 | 36,424 | 79, 66, 69 | 15 | 49 $Na^+$ |

The PDB ids of the structures providing the starting points are given in parentheses after the solute name.

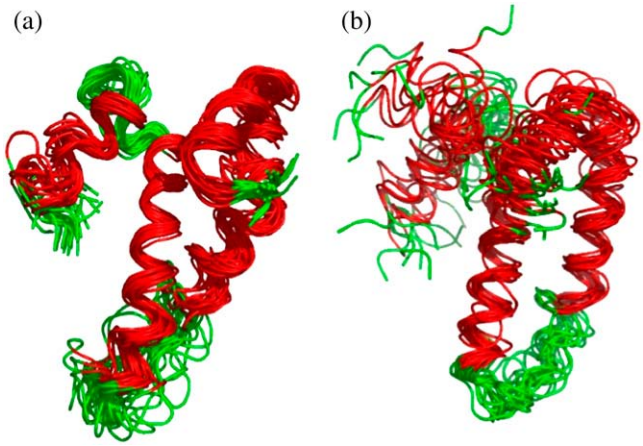


FIGURE 3 Conformers of the NMR structures 1ab3 (*a*) and 2fkx (*b*) shown in cartoons. The conformers are superposed to minimize the RMSD on the complete structure (*a*) or on residues 24–70 (*b*). The figure was realized with PyMOL 0.98 (61).

The relative orientations of the $\alpha$-helices show different patterns in 1ab3 and 2fkx (Table 4). The mean values of the angles between $\alpha1$ and $\alpha2$ and between $\alpha3$ and $\alpha4$ are smaller in 2fkx than in 1ab3: the helices $\alpha1$ and $\alpha4$ are thus less parallel to the protein core formed by $\alpha2$ and $\alpha3$. The standard deviations of angles between the axes of $\alpha$-helices in 1ab3 are much smaller than those observed in 2fkx. A similar trend is observed for the distances between the helix axes and particularly between the axes of $\alpha1$ and $\alpha2$. Thus, the helix $\alpha1$ and, to a lesser extent, the helix $\alpha4$ display a much wider range of orientations in 2fkx than in 1ab3. Because of the variability of the $\alpha1$ and $\alpha4$ orientations, larger RMSD values between the conformers of the complete protein are observed in the 2fkx than in the 1ab3 structure. But backbone RMSD values calculated by superimposing only the helices $\alpha2$ and $\alpha3$ of the protein (residues 24–70) are smaller for 2fkx than for 1ab3 (Table 2, part c).

**TABLE 3 Numbers of NOE restraint violations in the NMR structures (1ab3 and 2fkx) and in the MD trajectories (s15-pdb and s15-aria) recorded on the isolated protein**

| NOE restraints | 1ab3 | 2fkx | s15-pdb | s15-aria |
|---|---|---|---|---|
| *i,i* | 9 | 10 | 15 | 21 |
| *i,i*+1 | 15 | 8 | 8 | 10 |
| *i,i*+2 | 0 | 0 | 1 | 1 |
| *i,i*+3 | 5 | 3 | 9 | 9 |
| $\|i-j\| > 3$ | 19 | 6 | 37 | 27 |
| Total | 48 | 26 | 70 | 68 |

The violations are consistent violations, i.e., observed in >50% of the conformers. The trajectory names are those given in Table 1.

The large variability observed for the $\alpha1$ and $\alpha4$ orientations arises from the sparsity of the NOE restraints network. Indeed, among the 91 long-range NOE restraints, 8 are applied between $\alpha1$ and $\alpha2$, 6 between $\alpha1$ and $\alpha4$, and 4 between $\alpha2$ and $\alpha4$. In $\alpha1$, only one residue, Phe-14, located at the C-terminal end of the helix, is involved in interhelix interactions, whereas in $\alpha4$, five residues, Arg-76, Tyr-77, Leu-80, Lys-83, and Leu-84, are involved in restraints with other helices. It is thus not surprising that the orientation of $\alpha4$ with respect to the protein core is better defined than the orientation of $\alpha1$. Furthermore, between $\alpha2$ and $\alpha3$, which have the best-defined relative orientation, 21 restraints exist, and they involve 5 residues in each helix.

The mean orientations of the $\alpha$ helices were also compared (Table 4) in the NMR (1ab3 and 2fkx) and in the x-ray (1a32 and 1dk1) structures of S15 as well as in the S15 structures

**TABLE 2 Structural quality of the NMR conformers of S15 from Berglund et al. (5) (PDB id: 1ab3) and recalculated using the CNS-ARIA scripts (PDB id: 2fkx)**

| (a) | PROCHECK Core (%) | PROCHECK Allowed (%) | PROCHECK Generously allowed (%) |
|---|---|---|---|
| 1ab3 | 59.4 ± 2.9 | 32.6 ± 3.2 | 7.5 ± 1.9 |
| 2fkx | 82.8 ± 3.6 | 14.3 ± 2.9 | 1.5 ± 1.5 |
| | PROCHECK Nonallowed (%) | PROCHECK Mean numbers of bad contacts | |
| 1ab3 | 0.5 ± 0.6 | 18.1 ± 3.0 | |
| 2fkx | 1.4 ± 1.1 | 0.1 ± 0.3 | |
| (b) | WHATIF *Z* score Second-generation packing quality | WHATIF *Z* score Ramachandran plot appearance | WHATIF *Z* score $\chi$-1/$\chi$-2 rotamer normality |
| 1ab3 | –4.7 ± 0.3 | –6.4 ± 0.4 | –4.6 ± 0.3 |
| 2fkx | –0.6 ± 0.7 | –3.6 ± 0.7 | –0.1 ± 0.6 |
| | WHATIF *Z* score Backbone conformation | Mean numbers of bumps | |
| 1ab3 | –7.6 ± 1.0 | 104.1 | |
| 2fkx | –3.4 ± 1.4 | 12.0 | |
| (c) | Number of conformers | Backbone RMSD (Å) (residues 24–70) | NOE violations | Dihedral violations |
| 1ab3 | 26 | 3.1 | 48 | 13 |
| 2fkx | 18 | 2.1 | 26 | 18 |

The analysis was performed using PROCHECK v.3.5.4 (37) and WHATIF (38). The violations are consistent violations, i.e., observed in >50% of the conformers.

**TABLE 4 Geometry of the S15 tertiary structure in the NMR structures (1ab3 and 2fkx), in the x-ray structures (1a32 and 1dk1), and in the structures of S15 in two conformations of the ribosome of *E. coli* (2avy and 2aw7)**

| | Angle $\alpha$1-$\alpha$2 (degrees) | Angle $\alpha$2-$\alpha$3 (degrees) | Angle $\alpha$3-$\alpha$4 (degrees) |
|---|---|---|---|
| 1ab3 | 140.9 ± 6.6 | 159.3 ± 6.0 | 147.8 ± 5.3 |
| 2fkx | 104.8 ± 39.2 | 154.9 ± 14.5 | 139.7 ± 17.0 |
| 1a32 | 62.5 | 150.5 | 145.2 |
| 1dk1 | 140.0 | 153.0 | 149.1 |
| 2avy | 140.8 | 150.4 | 145.1 |
| 2aw7 | 141.8 | 150.1 | 143.1 |
| | Distance $\alpha$1-$\alpha$2 (Å) | Distance $\alpha$2-$\alpha$3 (Å) | Distance $\alpha$3-$\alpha$4 (Å) |
| 1ab3 | 9.2 ± 0.2 | 8.2 ± 0.4 | 7.3 ± 0.1 |
| 2fkx | 8.5 ± 1.2 | 9.7 ± 0.8 | 7.1 ± 0.3 |
| 1a32 | 21.1 | 9.3 | 7.4 |
| 1dk1 | 8.6 | 9.3 | 7.6 |
| 2avy | 8.2 | 9.0 | 7.3 |
| 2aw7 | 8.2 | 9.0 | 7.2 |

present in the 3.5 Å resolution x-ray structures (2avy and 2aw7) of the 70S ribosome of *E. coli* (42). The $\alpha$1-$\alpha$2 and $\alpha$2-$\alpha$3 angles of the 2fkx conformers are between the values observed in the structures 1a32 and 1ab3. The angles and the distances between the $\alpha$-helices in 1dk1, 2avy, and 2aw7 are close to those observed in 1ab3.

The backbone angles $\phi$ and $\psi$ of residues 15–23, which form the loop connecting the helices $\alpha$1 and $\alpha$2, exhibit quite different mean values in the NMR structures (1ab3, 2fkx), as well as in the x-ray structures (1a32, 1dk1, 2avy, 2a7w) (Fig. 4, *a* and *b*). Various conformations of the loop are thus observed in the different S15 structures.

The 2fkx conformers display a better structure quality and a lighter internal strain than those of the 1ab3 structure. Nevertheless, the convergence of the structure is worse: the orientations of the helices $\alpha$1 and $\alpha$4 with respect to the protein core are more variable in the 2fkx conformers. This feature is in agreement with the sparse network of long-range NOE restraints and with the x-ray structure of S15 (PDB id: 1a32), where the first helix is extended far apart from the other protein helices (6).

## MD simulations of the isolated protein S15

A name for each MD trajectory is given in Table 1, along with the main simulation parameters. In the two MD simulations recorded on the protein S15, the variation of the coordinate RMSD with respect to the starting point, shows different trends (Fig. 5 *a*). RMSD values larger than 7.0 Å are observed for s15-pdb, whereas values of about 4.5 Å are observed in the case of s15-aria. The protein conformation in s15-aria thus displays a better stability than that in s15-pdb, which is probably because of the lighter internal strain of the structure, observed in the previous section.

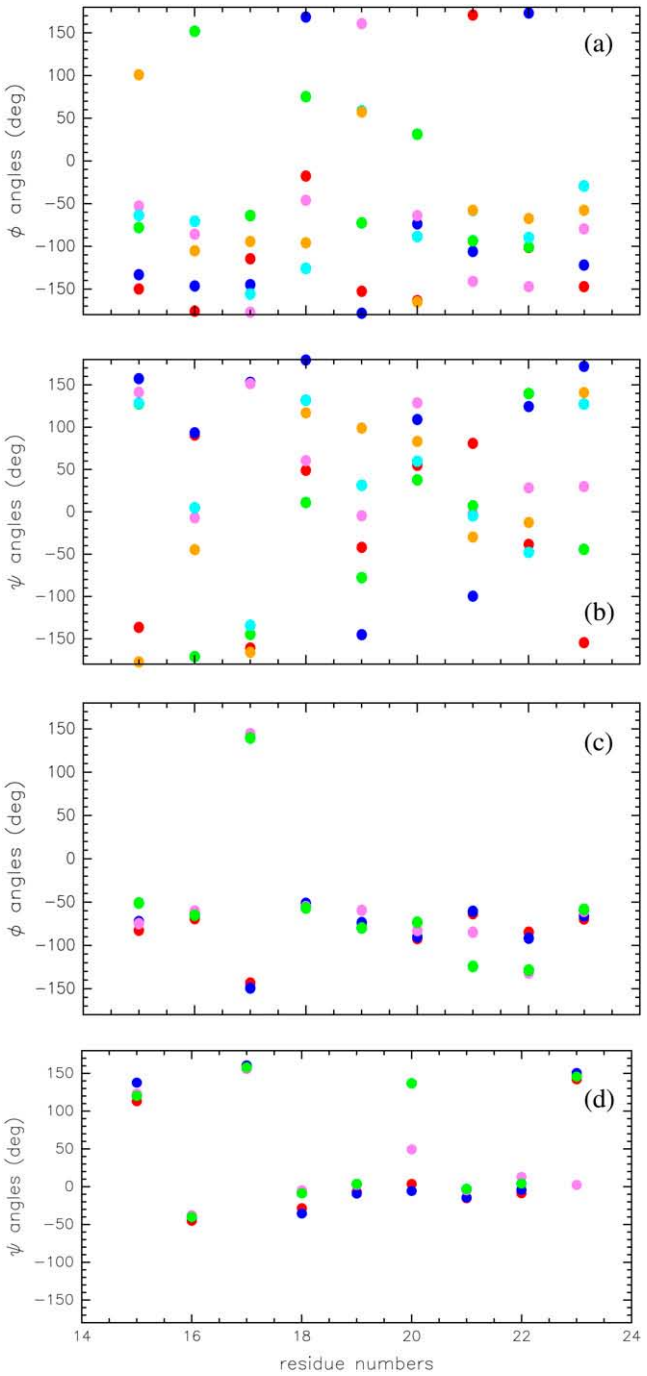


FIGURE 4 Mean values of the $\phi$ (*a* and *c*) and $\psi$ (*b* and *d*) angles in the loop connecting the $\alpha$1 and $\alpha$2 helices of S15. The angle values measured in the NMR and x-ray structures (*a* and *b*) and calculated during the 11–15-ns interval of the MD trajectories (*c* and *d*). These angle values are plotted along the residue numbers. (*a* and *b*) The color code is 1ab3 (*red*), 2fkx (*blue*), 1dk1 (*pink*), 1a32 (*green*), 2avy (*cyan*), and 2a7w (*orange*). (*c* and *d*) The color code is s15-pdb (*red*), s15-aria (*blue*), s15-rna-mg (*pink*), and s15-rna (*green*). The *x* axis describes the residue numbers, and the *y* axis the angle values in degrees.

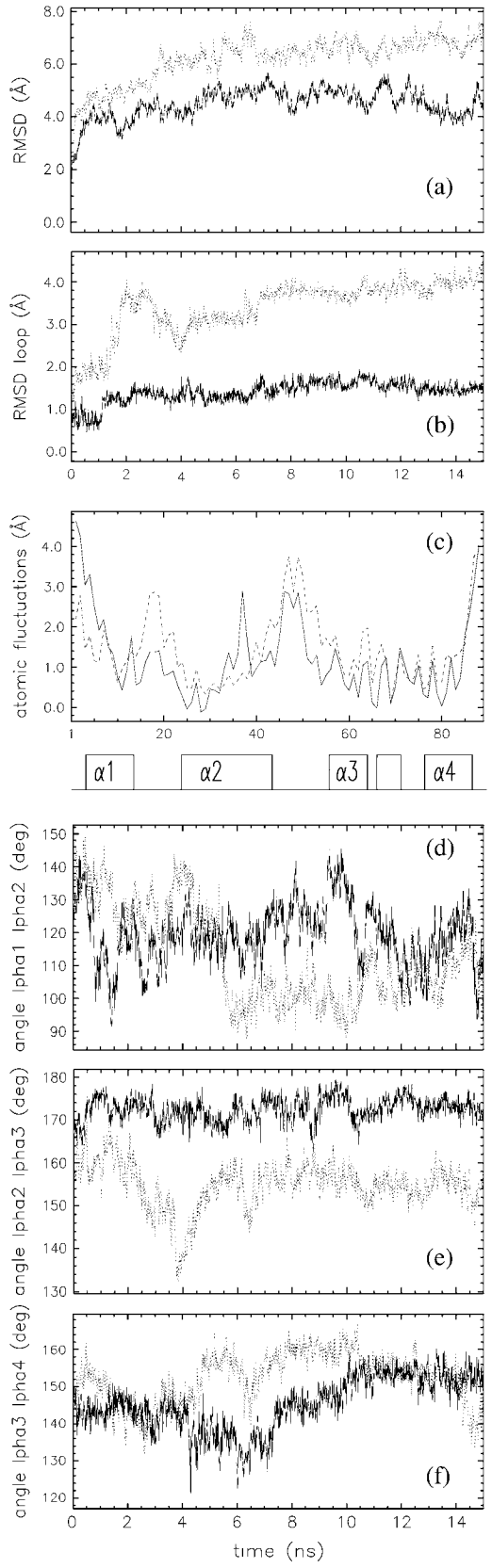


FIGURE 5 Comparison of trajectories s15-pdb and s15-aria. Coordinate RMSD from the starting point calculated on (*a*) all atoms or (*b*) the loop connecting helices $\alpha2$ and $\alpha3$ (residues 41–57). (*c*) Atomic fluctuations by residues. Angles between helices $\alpha1$,$\alpha2$ (*d*), $\alpha2$,$\alpha3$ (*e*), and $\alpha3$,$\alpha4$ (*f*). The full line is for the trajectory s15-aria, and the dotted/dashed lines for the trajectory s15-pdb. The *x* axis describes the trajectory time (ns) and the residue numbers, and the *y* axis describes the angle values (degrees) or the RMSD value and atomic fluctuations (Å). The secondary structures of S15 are shown below *c*.

The large RMSD values observed in the trajectory s15-pdb mainly arise from a conformational drift observed for the loop connecting the helices $\alpha2$ and $\alpha3$ (Fig. 5 *b*). RMSD values larger than 2.0 Å are also observed on the loop connecting $\alpha1$ and $\alpha2$, in the 2- to 4-ns interval (data not shown). The whole protein, except a few residues (residues 3–15 ($\alpha1$) and residues 35–40 ($\alpha2$)) consequently displays larger atomic fluctuations in s15-pdb than in s15-aria (Fig. 5 *c*). The differences in fluctuations are particularly large in the 15–25 and in the 42–52 regions, which correspond to the loops between helices $\alpha1$ and $\alpha2$ and between helices $\alpha2$ and $\alpha3$.

The angles between the helices $\alpha1$ and $\alpha2$ (Fig. 5 *d*) and $\alpha3$ and $\alpha4$ (Fig. 5 *f*) vary in the same range (90–140°) during both trajectories. This variability of the orientations of $\alpha1$ and $\alpha4$ with respect to the protein core is in agreement with the observations made above on 2fkx. On the other hand, the angle between $\alpha2$ and $\alpha3$ (Fig. 5 *e*) undergoes a transition in the nonstabilized part of the trajectory s15-pdb but is stable in the trajectory s15-aria.

The secondary structure elements have been monitored along the trajectories (data not shown) by calculating the mean and the standard deviation values of the backbone NH. . .O hydrogen bond distances in the $\alpha$ helices. In both trajectories, the helix $\alpha1$ (residues 3–15) is not well defined; nor are the C-terminal part of $\alpha2$ and the N-terminal part of $\alpha3$. The C-terminal regions of $\alpha3$ and $\alpha4$ are less stable in s15-pdb than in s15-aria.

The numbers of violations for the $(i, i + 1)$, $(i, i + 2)$, $(i, i + 3)$ NOE restraints are similar (Table 3) for both trajectories. On the other hand, s15-aria displays 7 more violations for the intraresidue $(i, i)$ NOEs, whereas 10 more violations are observed in s15-pdb for the long-range NOEs. The visualization of the violated NOEs on a contact map (Fig. 6) demonstrates that very long-range NOE restraints $(i, j)$ such that $|i - j| > 30$ are observed in s15-pdb but not in s15-aria. On the other hand, most of the $(i, j)$ NOE violations observed in s15-aria are such that $|i - j| < 10$. This distribution of the violations is in agreement with the larger conformational drift observed in s15-pdb than in s15-aria.

The observations quoted above show that the trajectory starting from a 2fkx conformer is more stable than the one recorded from a 1ab3 conformer. This is probably because of the calculation of the 2fkx structure in the torsion angle space as well as the use of a final refinement step in water, as it was shown (35,39,41) that these two ingredients improve the quality of the structure and thus the stability in MD

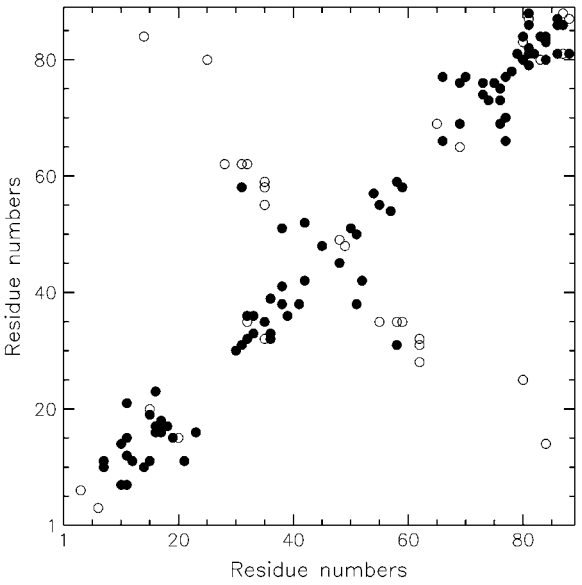


FIGURE 6 Contact plot of the violated NOEs during the trajectories of the isolated protein S15 (*open circles*, s15-pdb; *solid circles*, s15-aria). The *x* and *y* axes describe the residue numbers.

simulation. On the other hand, the better convergence of 1ab3, which is the sign of a larger internal strain of the structure, is correlated to a larger conformational drift in the s15-pdb simulation (43).

The variable orientations observed for the helices in S15 may arise from the bundle helix structure of the protein S15. Indeed, in $p8^{MTPC1}$ (44), a protein consisting of three $\alpha$-helices and having a similar tertiary structure, the third helix displays internal motion and large displacements in MD simulations (45), and this behavior is in agreement with dipolar coupling measurements (46).

## Internal mobility in the S15-RNA complex

The mobility of the partners of S15-RNA interaction was analyzed during the trajectories s15-rna-mg and s15-rna, by calculating separately on S15 and on RNA the atomic fluctuations by residues from the 11–15-ns interval of the trajectories. In the protein, a slight increase of fluctuations is observed in absence of $Mg^{2+}$ (Fig. 7 *a*) for residues 37–50 in helices $\alpha$2 and $\alpha$3 and in the loop connecting them.

In absence of $Mg^{2+}$, an increase of flexibility of RNA is observed in four regions (Fig. 7 *b*): residues 92–100 (588–650) in the TL1 tetraloop, residues 102–104 (652–654) and 133–134 (748–749) near the three-way junction, residue 115 (665) close to the G-U/G-C motif, and residues 121–123 in the TL2 tetraloop. Among these residues, A103 (653), A115 (665), and C133 (748) are not involved in canonical base-pairs in the structure 1dk1. The increase of RNA fluctuations is in agreement with the positions of the $Mg^{2+}$ ions in the crystal, close to the G-U/G-C motif and to the three-way junction motif. The increases of flexibility observed in protein helices $\alpha$2 and $\alpha$3, in the $\alpha$2-$\alpha$3 loop (Fig. 7 *a*), and in the TL2 tetraloop (Fig. 7 *b*), are consistent because these regions interact.

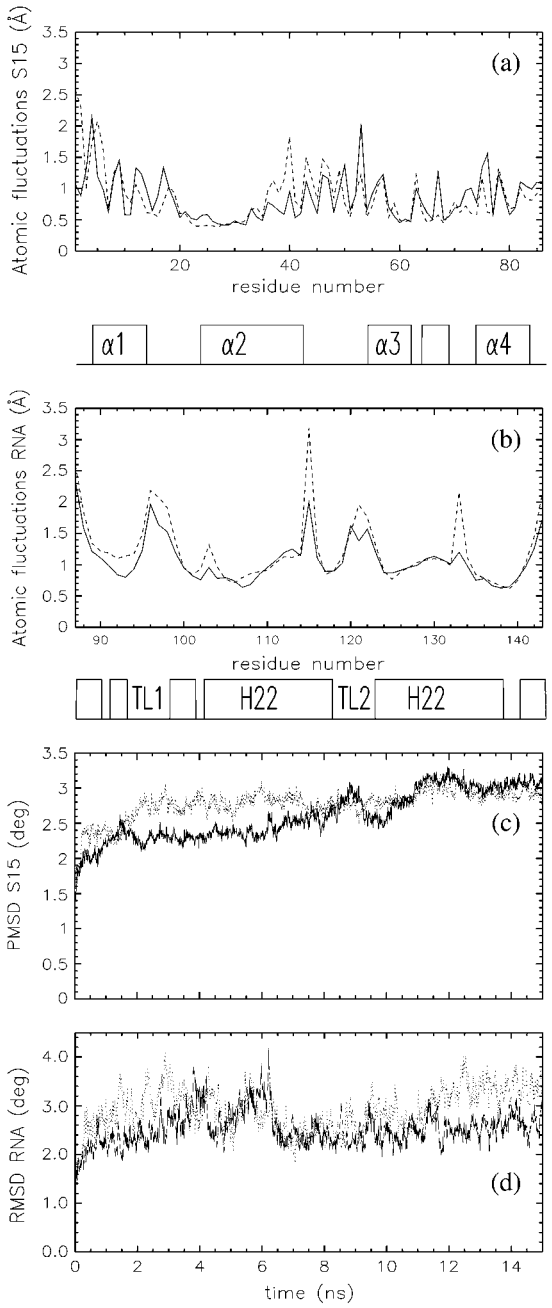


FIGURE 7 Comparison of the trajectories s15-rna-mg and s15-rna. Atomic fluctuations by residues in S15 (*a*) and in RNA (*b*), calculated on the time interval 11-15 ns. The RMSD values from the starting point are calculated on (*c*) all atoms in S15 or (*d*) all atoms in RNA. The full line is for the trajectory s15-rna, and the dotted/dashed lines for the trajectory s15-rna-mg. The *x* axis describes the trajectory time (ns) or the residue numbers, and the *y* axis describes the atomic fluctuations (Å) or the RMSD (Å). The secondary structures of S15 and RNA are shown below *a* and *b*.

## Conformational drift of S15

In the presence of $Mg^{2+}$ ions, the RMSD of S15 atomic coordinates from the initial conformation converges to a plateau of 3 Å after 11 ns (Fig. 7 *c*). The trajectory recorded in the absence of $Mg^{2+}$ ions reaches the same value after 3 ns (Fig. 7 *c*). The variation of the coordinate RMSD of the protein S15 in the presence of $Mg^{2+}$ displays a jump in the 7.8- to 11.5-ns range (Fig. 7 *a*) before attaining the plateau value. The conformations corresponding to the minimum RMSD values in this interval (7881 ps: 2.31 Å, 9895 ps: 2.41 Å) were compared (Fig. 8 *a*) with the conformations corresponding to the maximum RMSD values (8837 ps: 3.11 Å, 11,347 ps: 3.29 Å). The conformation of the $\alpha1$-$\alpha2$ loop changes, and residues 15–19 undergo the largest displacement (Fig. 8 *b*). Residues 3–7 move simultaneously (Fig. 8 *c*), and the backbone hydrogen bond between Lys-4 and Gln-8 is disrupted. The simultaneous variation of conformation for residues 3–7 and 15–19 is consistent with a mechanical link between the loop connecting helices $\alpha1$ and $\alpha2$ and helix $\alpha1$.

Because the $\alpha1$-$\alpha2$ loop is located at the intermolecular interface of the S15-RNA complexes in the crystal, the loop conformation is probably disturbed by crystal packing effects. The loop drifts during all MD trajectories, recorded on the S15-RNA complex and on S15, as similar mean $\phi$ and $\psi$ values are calculated from the whole MD trajectories in the loop connecting $\alpha1$ and $\alpha2$ (Fig. 4, *c* and *d*), whereas different values are observed in the different NMR and x-ray structures (Fig. 4, *a* and *b*). Transitions of the $\phi$ and $\psi$ values are thus observed (Fig. 9) in residues located in the $\alpha1$-$\alpha2$ loop, in the presence or in the absence of $Mg^{2+}$ ions.

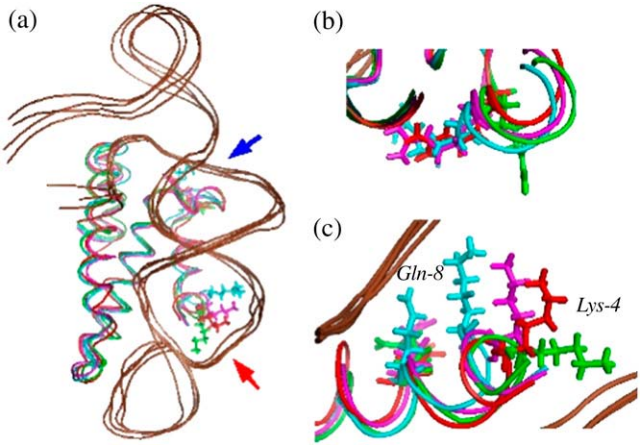


FIGURE 8 Superposition of the S15-RNA conformations recorded at 7881, 8837, 9895, and 11,347 ps in the presence of $Mg^{2+}$ ions. The RNA is in brown, and the S15 conformers are in cyan (7881 ps), green (8837 ps), magenta (9895 ps), and red (11,347 ps). (*a*) The full complex structure is shown in cartoon. A blue arrow indicates the $\alpha1$-$\alpha2$ loop and a red arrow the N-terminal region. The residues Arg-16 and Lys-4 are drawn in sticks. (*b*) Zoom on the loop linking $\alpha1$ and $\alpha2$, with Arg-16 drawn in sticks. (*c*) Zoom on the N-terminal part of $\alpha1$ with Lys-4 and Gln-8 drawn in sticks. This figure was realized with PyMOL 0.98 (61).

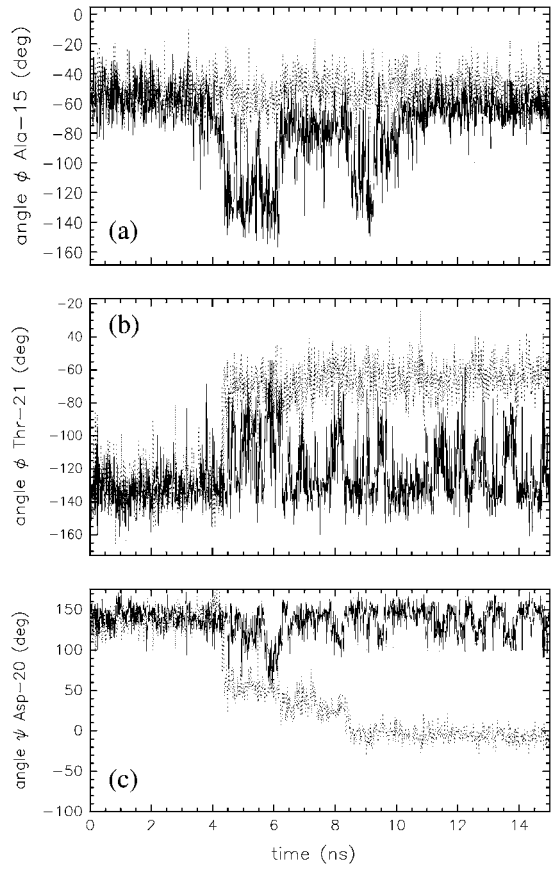


FIGURE 9 Variation of the angles (*a*) $\phi$ of Ala-15, (*b*) $\phi$ of Thr-21, and (*c*) $\psi$ of Asp-20 in the loop connecting the helices $\alpha1$ and $\alpha2$ in S15. The full line is for the trajectory s15-rna, and the dotted line for the trajectory s15-rna-mg. The *x* axis describes the trajectory time (ns), and the *y* axis describes the angle values (degrees).

The angles between the S15 helices and the distances separating them vary $<10°$ and 1 Å, respectively (data not shown), during the trajectories s15-rna-mg and s15-rna: the presence of RNA freezes the variability of the helices' orientations, observed for the isolated protein. Nevertheless, the angle between $\alpha2$ and $\alpha3$ is increased by 6° if the $Mg^{2+}$ ions are removed, and because the helices are antiparallel, they are thus further apart in the presence of $Mg^{2+}$ ions. Also, when the $Mg^{2+}$ ions are removed, the distance between $\alpha1$ and $\alpha2$ is reduced by 1 Å after 10 ns.

## RNA conformation

The variation of the coordinate RMSD of the RNA in presence of $Mg^{2+}$ displays two jumps at around 4 and 6 ns (Fig. 7 *b*). The conformations exhibiting the maximum RMSD values (3812 ps: 3.82 Å, 6212 ps: 4.22 Å) were compared to conformations exhibiting the minimum RMSD values (3261 ps: 2.20 Å, 4782 ps: 2.01 Å, 6347 ps: 2.28 Å). The 3′ and 5′ extremities spanning the 87–90 (584–586) and 140–143 (755–757) residues exhibit different conformations.

The interphosphate distances between phosphate groups facing each other in the RNA backbone were calculated on the 11–15-ns interval of the trajectories s15-rna-mg and s15-rna. All distance differences are smaller than 1.5 Å, except the four following ones. The pairs of residues A113(663)-G127(742), G114(664)-G126(741), G116(666)-U125(740), and U119-G122 show variations of distance of 2.0 Å, 2.1 Å, 2.0 Å, and 4.6 Å. These residues are located in the G-U/G-C region and in tetraloop TL2. The phosphate groups thus move apart in the absence of $Mg^{2+}$ ions, which is in agreement with the increase of internal flexibility in this RNA region (Fig. 7 *b*).

The values of the RNA phosphodiester angles were compared in the presence and in the absence of $Mg^{2+}$ ions, by calculating their mean and standard deviation values in the 11–15-ns interval (Fig. 10). Few angles display a difference of mean values significant with respect to the standard deviation values. These differences concern, for the angle $\alpha$, 11 residues, for the angle $\beta$, 1 residue, for the angle $\gamma$, 7 residues, for the angle $\delta$, 6 residues, for the angle $\varepsilon$, 6 residues, and for the angle $\zeta$, 4 residues. These residues cluster in the UUCG TL2 tetraloop, in the three-way junction, and in the helix H22, close to the positions of the $Mg^{2+}$ ions. These phosphodiester angle variations are thus in agreement with the stabilization of the RNA structure by the $Mg^{2+}$ ions (2). But the hydrogen bond parameters (data not shown) involved in a base triple among G104(654), G137(752), and C139(754) are not modified between s15-rna and s15-rna-mg.

Comparison of the mean angle values from the trajectories with the corresponding angles measured in 1dk1 shows (Fig. 10) that, for the majority of the residues, the trajectories' angles are in a similar angular region than the values observed in the structure. The x-ray angles were compared to the interval of variation of the trajectory angles, and the residues for which the x-ray angle is more than 90° outside of the interval are the following ones: G92 (588), U102 (652), G107(657), A113(663), G114(664), A115(665), U120, G122, G123, U125(740), G127(742), C133(748), C134(749), G135 (750), A138(753), and C143.

The angle values calculated on the trajectories and measured on the 1dk1 structure were also compared to the rotameric classification introduced recently (47) to describe the RNA backbone. The mean absolute difference value between the RNA angles and the rotameric angles was calculated over the 53 sugar-to-sugar angle suites present in the RNA. For each pair of angle values $p$ and $q$, the difference was the smallest absolute value of the three numbers: $p-q$, $p-q+360°$ and $p-q-360°$. The RX structure of S15-RNA displays 18 suites with means difference larger than 20°, and the maximum mean difference observed is 79.9°. On the other hand, the s15-rna-mg and s15-rna trajectories have 10 and 13 such suites, and their maximum mean differences are 46.4° and 73.8° The conformations explored during the 11–15-ns trajectory intervals thus seem to be in reasonable agreement with the analysis of rotamers performed on 132 RNA crystallographic structures (47).

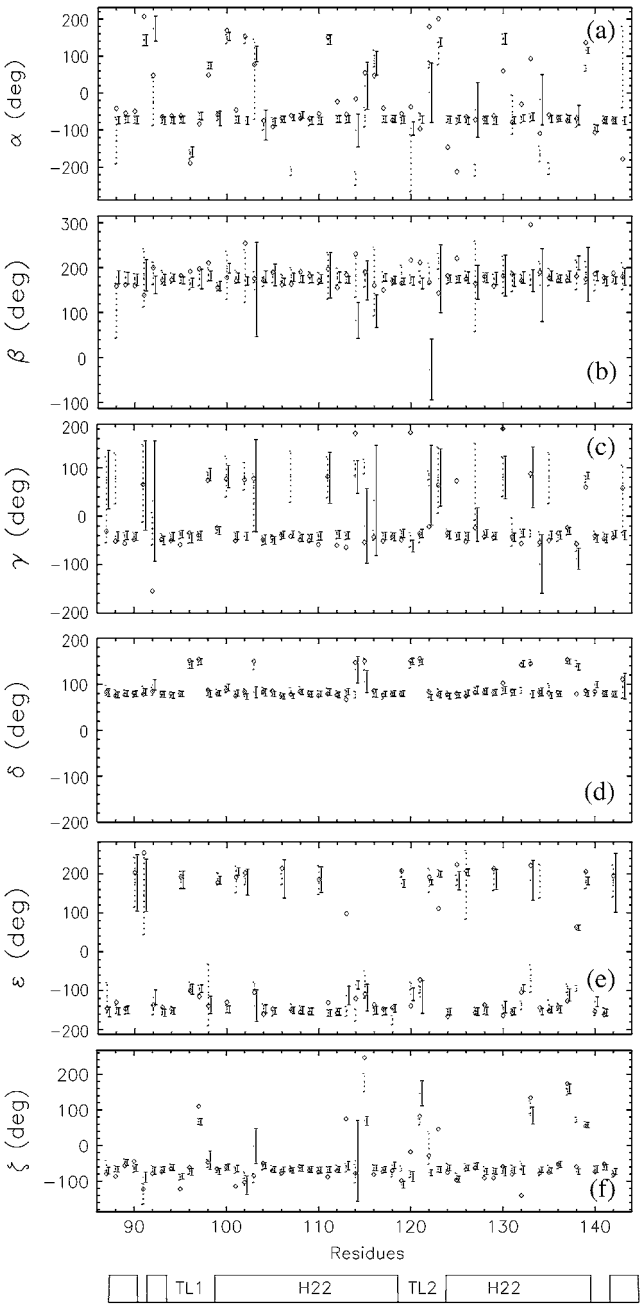


FIGURE 10 Angles of the RNA phosphodiester backbone ((*a*) $\alpha$, (*b*) $\beta$, (*c*) $\gamma$, (*d*) $\delta$, (*e*) $\varepsilon$, and (*f*) $\zeta$). The mean values and the standard deviations, calculated on the 11–15-ns range, are given along the residue number (*dashed line*, s15-rna-mg; *solid line*, s15-rna). The angle values measured on the 1dk1 structure are shown by diamonds. The secondary structures of RNA are shown at the bottom.

The simulation of UUCG loops was used as a test case in MD simulations (48,49); the first NMR structure of the UUCG loop (50) was incorrect and was corrected (51) by discovering a misassignment. The use of combined locally enhanced sampling and Particle Mesh Ewald was shown (49) to allow the simulation to find the correct structure starting from the incorrect one. However, several simulations (48) of the two

UUCG structures concluded with the formation of the hydrogen bond U1(O2′)-U2(O5′) and not U1(O2′)-G4(O6).

The conformation of the two UUCG tetraloops was compared (Fig. 11) to experimental structures of UUCG (1dk1, 1f7y, 1hlx, 1i6u, 1kuq). The structure 1hlx is the NMR structure of the P1 helix from group I self-splicing introns (51), in which only one UUCG loop is present. The others are the S15-RNA (3,4) and S18-RNA (52) x-ray structures in which a three-way-junction RNA is present, with both tetraloops TL1 and TL2. The values of the phosphodiester backbone angles are similar in structures and in MD trajectories. The angles displaying the largest variations between s15-rna-mg and s15-rna also vary among the experimental structures.

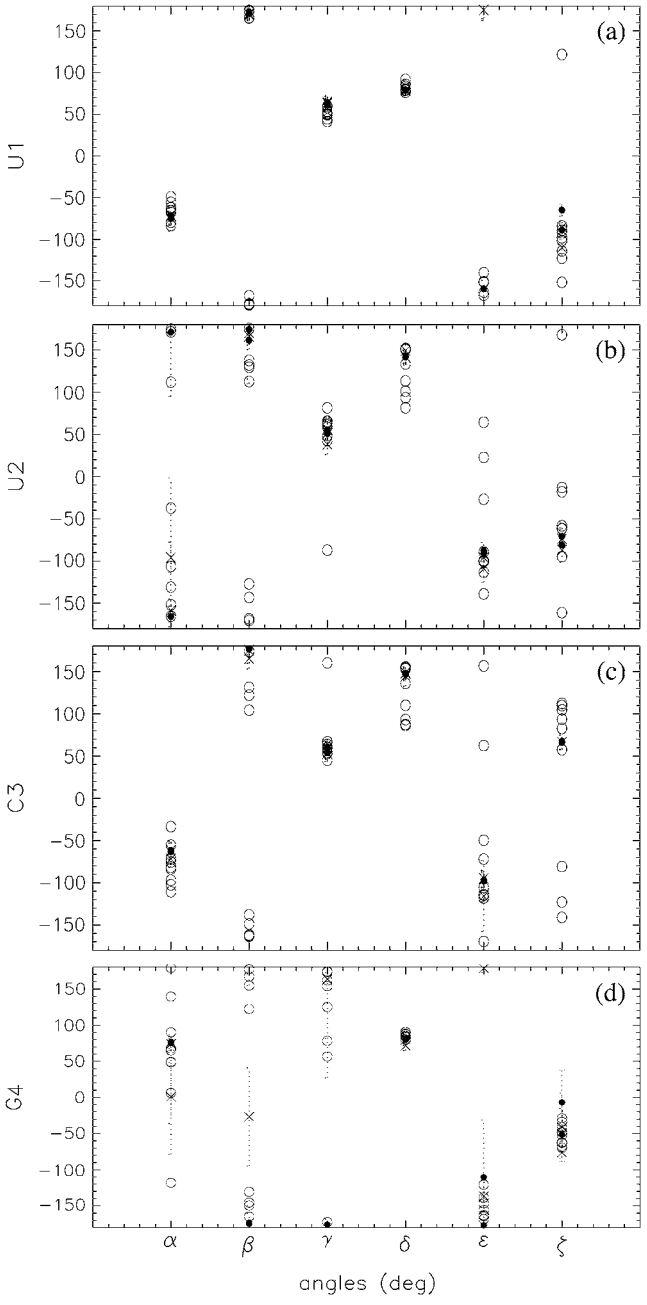


FIGURE 11 Values of the phosphodiester backbone angles for the U1 (*a*), U2 (*b*), C3 (*c*), and G4 (*d*) residues in UUCG tetraloops. The values obtained for the PDB files (1dk1 (3), 1f7y (4), 1hlx (51), 1i6u (52), 1kuq) are shown with open circles. The values calculated from the 11–15-ns intervals in s15-rna-mg and s15-rna are shown with dots and crosses, respectively. For the PDB file 1hlx and the MD trajectories, the mean values of the angles are shown, along with the standard deviations as dotted lines.

A set of hydrogen bonds already analyzed in a MD simulation of UUCG (48) was compared in the MD trajectories and in x-ray and NMR UUCG structures (Table 5). The comparison between TL1 and TL2 inside the MD trajectories shows that in s15-rna-mg, over nine distances, five show a difference larger than 1 Å, whereas in s15-rna, only two distances show a difference larger than 1 Å. This reduction in the number of differences is in agreement with the homogenization of the environment of the UUCG loops obtained by removing the $Mg^{2+}$ ions. The loop TL1 shows the same pattern of formed hydrogen bonds in both MD trajectories, but the percentage of hydrogen bond formation generally decreases in absence of $Mg^{2+}$.

The comparison between the MD trajectories and the structures gives the following results. The pattern of formed hydrogen bonds in TL1 is qualitatively similar to those obtained for TL1 in x-ray and NMR structures. In TL2, the distances vary much between the x-ray structures, and consequently, the formation of the hydrogen bond observed in the MD trajectories is always in agreement with a least one x-ray structure. The hydrogen bond between U1(O2′) and G4(O6) is partially formed in TL1 but not in TL2 for s15-rna-mg. In all x-ray structures, this hydrogen bond is formed in TL1, but in the NMR structure, it is partially formed.

The hydrogen bond between U1(O2′) and U2(O5′) is stronger than the one between U1(O2′) and G4(O6) for TL1 and TL2 in both s15-rna trajectories. This observation is in agreement with that of Miller and Kollman (48) but contradicts the observations made on the x-ray structures, as already pointed out by Ennifar et al. (4). Nevertheless, the analysis of the NMR structure 1hlx shows that the hydrogen bonds between U1(O2′) and G4(O6) and U1(O2′) and U2(O5′) are both partially formed in the NMR structure, with formation percentages of the same order of value. In all x-ray structures, the UUCG loop is included in a larger RNA sequence. On the other hand, the only structure of an isolated UUCG loop is the NMR structure 1hlx. The nonavailability of a crystallized structure for this molecule may be the sign of a large internal flexibility, which is also observed in MD trajectories.

The previous analysis of the hydrogen bonds inside loops UUCG showed that the removal of $Mg^{2+}$ ions induces a reorganization of the hydrogen bond network, but according to the limitation of the modeling of ion electrostatics, it is not possible to state that this behavior is specific of $Mg^{2+}$ ions. One should also notice that 1), the $Mg^{2+}$ ions observed in the S15-RNA crystal may not all have to be present, 2), in the NMR sample of the P1 helix from group I self-splicing introns, no $Mg^{2+}$ ions were present, but other ions were

**TABLE 5 Parameters of hydrogen bonds in UUCG loops calculated on the 11–15-ns time interval of the trajectories s15-rna-mg and s15-rna and on PDB structures (1dk1 (3), 1f7y (4), 1hlx (51), 1i6u (52), 1kuq)**

| Hydrogen bond | Distance (Å) | Angle (degrees) | Formation (%) |
|---|---|---|---|
| s15-rna-mg | | | |
| TL1 U1(O2) G4(N2/H21) | 2.4 ± 0.4 | 139.5 ± 12.8 | 45.9 |
| TL1 U2(O2P) C3(N4/H41) | 3.8 ± 0.4 | 37.8 ± 6.7 | 0 |
| TL1 U1(O2) G4(N2/H22) | 4.0 ± 0.4 | 25.6 ± 7.7 | 0 |
| TL1 U2(O2P) C3(N4/H42) | 2.1 ± 0.4 | 155.3 ± 13.2 | 77.3 |
| TL1 U1(HO′2) G4(O6) | 3.9 ± 0.9 | 57.3 ± 42.4 | 12.9 |
| TL1 U1(HO′2) U2(O5′) | 2.5 ± 0.72 | 40.1 ± 37.5 | 46.4 |
| TL1 U1(H3) G4(O6) | 6.3 ± 0.4 | 74.1 ± 6.1 | 0 |
| TL1 U1(O2) G4(N1) | 1.9 ± 0.2 | 153.3 ± 12.1 | 90.1 |
| TL1 U1(O4) G4(N1) | 6.3 ± 0.3 | 147.4 ± 10.3 | 0 |
| TL2 U1(O2) G4(N2/H21) | 6.6 ± 0.7 | 72.4 ± 6.8 | 0 |
| TL2 U2(O2P) C3(N4/H41) | 3.7 ± 0.2 | 37.8 ± 5.2 | 0 |
| TL2 U1(O2) G4(N2/H22) | 7.1 ± 0.7 | 41.6 ± 7.3 | 0 |
| TL2 U2(O2P) C3(N4/H42) | 2.0 ± 0.2 | 162.2 ± 8.7 | 88.5 |
| TL2 U1(HO′2) G4(O6) | 6.1 ± 0.9 | 53.3 ± 41.7 | 0 |
| TL2 U1(HO′2) U2(O5′) | 3.1 ± 0.6 | 59.7 ± 28.9 | 1.2 |
| TL2 U1(H3) G4(O6) | 6.3 ± 0.4 | 74.1 ± 6.1 | 0 |
| TL2 U1(O2) G4(N1) | 4.9 ± 0.6 | 62.1 ± 7.1 | 0 |
| TL2 U1(O4) G4(N1) | 8.0 ± 0.4 | 45.4 ± 5.8 | 0 |
| s15-rna | | | |
| TL1 U1(O2) G4(N2/H21) | 2.1 ± 0.3 | 148.9 ± 13.7 | 75.4 |
| TL1 U2(O2P) C3(N4/H41) | 3.7 ± 0.4 | 38.2 ± 6.6 | 0 |
| TL1 U1(O2) G4(N2/H22) | 3.8 ± 0.3 | 31.0 ± 9.3 | 0 |
| TL1 U2(O2P) C3(N4/H42) | 2.0 ± 0.4 | 159.6 ± 11.1 | 86.8 |
| TL1 U1(HO′2) G4(O6) | 4.5 ± 0.6 | 49.7 ± 19.1 | 2.0 |
| TL1 U1(HO′2) U2(O5′) | 2.4 ± 0.4 | 34.4 ± 17.2 | 26.9 |
| TL1 U1(H3) G4(O6) | 6.6 ± 0.5 | 79.1 ± 6.5 | 0 |
| TL1 U1(O2) G4(N1) | 2.2 ± 0.4 | 144.7 ± 12.8 | 62.5 |
| TL1 U1(O4) G4(N1) | 6.6 ± 0.4 | 136.8 ± 11.3 | 0 |
| TL2 U1(O2) G4(N2/H21) | 2.6 ± 0.5 | 131.6 ± 11.8 | 23.7 |
| TL2 U2(O2P) C3(N4/H41) | 4.0 ± 0.8 | 39.7 ± 6.9 | 0 |
| TL2 U1(O2) G4(N2/H22) | 4.3 ± 0.4 | 20.0 ± 7.2 | 0 |
| TL2 U2(O2P) C3(N4/H42) | 2.3 ± 0.8 | 162.4 ± 9.8 | 67.2 |
| TL2 U1(HO′2) G4(O6) | 7.5 ± 0.5 | 31.5 ± 14.4 | 0 |
| TL2 U1(HO′2) U2(O5′) | 2.4 ± 0.3 | 30.8 ± 16.5 | 28.1 |
| TL2 U1(H3) G4(O6) | 3.8 ± 0.3 | 132.7 ± 9.3 | 0 |
| TL2 U1(O2) G4(N1) | 1.9 ± 0.1 | 158.6 ± 10.6 | 96.8 |
| TL2 U1(O4) G4(N1) | 5.8 ± 0.3 | 149.5 ± 8.5 | 0 |

| | 1dk1 (Å) | 1f7y (Å) | 1i6u (Å) | 1kuq (Å) |
|---|---|---|---|---|
| TL1 U1(O2) G4(N2) | 3.3 | 3.3 | 3.7 | 2.8 |
| TL1 U2(O2P) C3(N4) | 2.9 | 3.0 | 2.9 | 3.4 |
| TL1 U1(O2′) G4(O6) | 2.5 | 2.4 | 2.8 | 2.5 |
| TL1 U1(O2′) U2(O5′) | 3.7 | 3.7 | 3.6 | 4.4 |
| TL1 U1(N3) G4(O6) | 5.9 | 5.9 | 5.8 | 6.3 |
| TL1 U1(O2) G4(N1) | 2.8 | 2.9 | 2.9 | 2.8 |
| TL1 U1(O4) G4(N1) | 7.0 | 7.0 | 6.9 | 7.1 |
| TL2 U1(O2) G4(N2) | 4.8 | 3.2 | 3.5 | 7.5 |
| TL2 U2(O2P) C3(N4) | 2.6 | 2.7 | 2.9 | 7.6 |
| TL2 U1(O2′) G4(O6) | 4.6 | 3.0 | 2.6 | 3.7 |
| TL2 U1(O2′) U2(O5′) | 3.8 | 3.9 | 5.0 | 4.0 |
| TL2 U1(N3) G4(O6) | 3.2 | 6.5 | 5.9 | 5.5 |
| TL2 U1(O2) G4(N1) | 3.0 | 3.2 | 3.0 | 5.3 |
| TL2 U1(O4) G4(N1) | 7.0 | 7.3 | 7.1 | 9.7 |

(*Continued*)

**TABLE 5 (*Continued*)**

| 1hlx | Distance (Å) | Angle (degrees) | Formation (%) |
|---|---|---|---|
| TL1 U1(O2) G4(N2/H21) | 3.9 ± 0. | 27.6 ± 3.2 | 0 |
| TL1 U2(O2P) C3(N4/H41) | 3.8 ± 1.1 | 131.5 ± 5.5 | 0 |
| TL1 U1(O2) G4(N2/H22) | 2.1 ± 0.2 | 145.5 ± 5.8 | 65 |
| TL1 U2(O2P)C3(N4/H42) | 5.2 ± 1.1 | 40.5 ± 2.9 | 0 |
| TL1 U1(HO′2) G4(O6) | 2.7 ± 0.3 | 72.5 ± 18.9 | 15 |
| TL1 U1(HO′2) U2(O5′) | 3.0 ± 0.4 | 84.0 ± 26.8 | 10 |
| TL1 U1(N3) G4(O6) | 6.6 ± 0.2 | 61.3 ± 2.1 | 0 |
| TL1 U1(O2) G4(N1) | 2.0 ± 0.1 | 153.7 ± 6.8 | 90 |
| TL1 U1(O4) G4(N1) | 6.5 ± 0.1 | 158.8 ± 7.0 | 0 |

The hydrogen bond mean distance is given as well as the donor-hydrogen-acceptor mean angle when available. The formation is the percentage of trajectory time or of NMR conformers in which the mean distance is <2.2 Å.

present (G. Varani, University of Washington, personal communication, 2006). The comparison among the MD trajectories and the x-ray and NMR structures reveals that floppier hydrogen bonds are generally observed in the NMR structure, which agrees with the observations made during the MD trajectories. Furthermore, the large heterogeneity of distances in TL2 agrees with the larger number of disrupted hydrogen bonds in TL2 during the MD trajectories. The overall analysis performed on the phosphodiester backbone angles and on the hydrogen bonds in TL1 and TL2 shows that the overall topology of the simulated TLs did not change much with respect to the crystallographic structures.

The relative positions of the three RNA helices forming the three-way junction were monitored (Fig. 12) by calculating the two angles formed by the atom triplets (107-C6, 114-N2, 142-O2) and (107-C6, 114-N2, 98-N1). The first angle describes the relative orientation of helices H22 and H20, and the second angle describes the relative orientation of helices H22 and H21. Both angles are slightly larger in the absence of $Mg^{2+}$ ions, which means that the helices have a tendency to go apart, in agreement with the observations of Batey and Williamson (2).

## Positions of the counterions and of the water bridges

The positions of the nine crystallographic $Mg^{2+}$ ions (Fig. 13) were analyzed along the full trajectory s15-rna-mg by determining, for each snapshot, the atoms forming the coordination cage of the $Mg^{2+}$ ions. The six oxygens closest to each $Mg^{2+}$ were determined for each snapshot. Table 6 describes the coordination partners of each $Mg^{2+}$ion along with their residence times.

The partners of $Mg^{2+}$ ions do not vary during the simulation. The only exception is the ion Mg-151: it interacts in the initial conformation with the atoms O1P and O2P of G107 (657), but the hydrogen bond with O2P is broken after 60 ps. This stability of the partners of $Mg^{2+}$ ions during the simulation shows that the simple model used for the $Mg^{2+}$ electrostatics can nevertheless give a description of

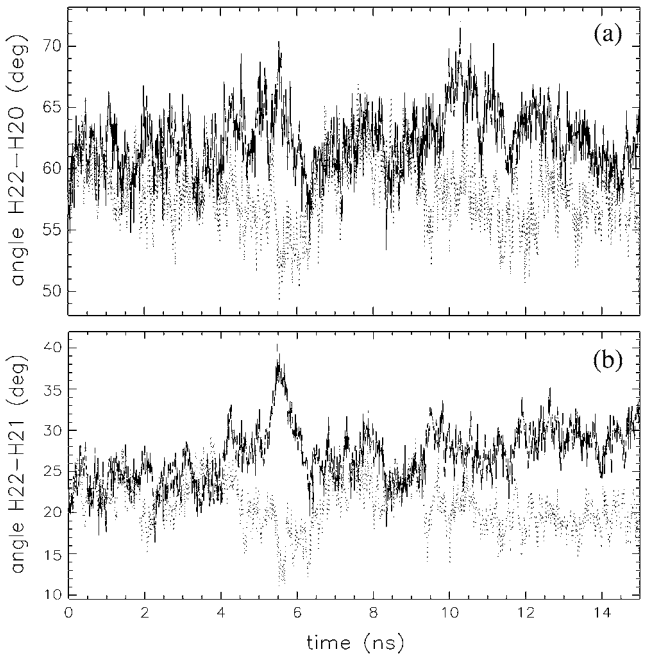


FIGURE 12 Variation of the angles (*a*) between H22 and H20 and (*b*) between H22 and H21 in the RNA during the MD trajectories of the complex. The full line is for the trajectory s15-rna and the dotted line for the trajectory s15-rna-mg. The two angles formed by the atom triplets (107-C6, 114-N2, 142-O2) and (107-C6, 114-N2, 98-N1) are plotted in degrees, according to the trajectory time. The first angle describes the relative orientation of the helices H22 and H20, and the second angle describes the relative orientation of the helices H22 and H21. The *x* axis describes the trajectory time (ns), and the *y* axis describes the angle values (degrees).

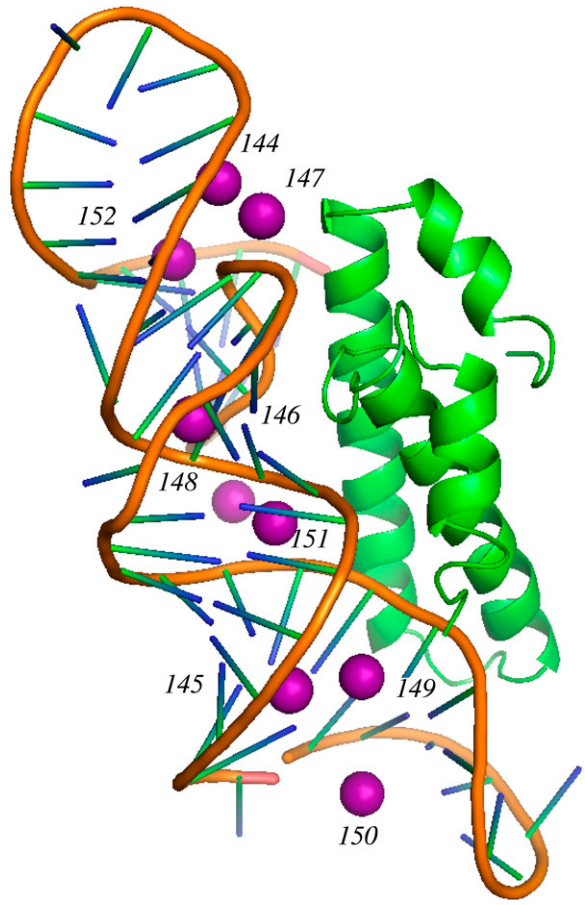


FIGURE 13 Structures of the S15-RNA complex (x-ray (1dk1) with the $Mg^{2+}$ ions drawn in *cpk*). The structures are shown in cartoon, the RNA backbone is brown, the RNA bases are cyan, and S15 is green. This figure was realized with PyMOL 0.99 (61).

the system in agreement with the x-ray crystallographic measurements.

Ion 144 is coordinated by five water oxygens with mean values of coordination distances around 2.0 Å. The sixth coordination partner of Mg-144 is always at a distance of ~3.7 Å and is quite variable. The two most frequent coordination partners are O6-99 (7.5 ns) and O2P-99 (1.1 ns). The ions Mg-145 and Mg-151 are hexacoordinated with five oxygens of water molecules and a phosphate oxygen (for Mg-145: O2P-G112 (662); for Mg-151: O1P-G107 (657)). The Mg-146 ion is hexacoordinated with four oxygens of water molecules and two atoms O6 of bases G107 (657) and G135 (750). The Mg-147, Mg-148, Mg-149, and Mg-150 ions are hexacoordinated with oxygens of water molecules. The Mg-152 ion is hexacoordinated with five water oxygens and the ribose oxygen O2′ in residue A138 (753). The direct interactions of the $Mg^{2+}$ ions are thus established mainly with water, phosphate, or O6 oxygens, which corresponds to the observations previously made in MD simulations (18,53). The distances between the atoms involved in the coordination cage of the magnesium ions have a mean standard deviation of 0.1 Å; the geometry of the coordination complex does not vary; and the oxygens form a rigid cage around the $Mg^{2+}$ ion, as observed by Auffinger et al. (19). The few direct interactions of the $Mg^{2+}$ ions with RNA residues involve G135 (750), A138 (753), and G107 (657), which are located in the vicinity of the hinge among helices H20, H21, and H22.

The water molecules forming the coordination cage of the $Mg^{2+}$ ions were then analyzed to detect their hydrogen bond partners. The residues Gln-61 and Asp-73 of S15 and the residues G91 (587), G92 (588), C93 (589), C94 (590), U95, G99 (649), A103 (653), G108 (658), G116 (666), G117 (667), C118, U119, G122, U125 (740), G127 (742), U128 (743), C133 (748), and G137 (752) of RNA are bound to a magnesium cluster more than 1 ns. These RNA residues are located in the H22 helix on the side not interacting with the protein and close to the G-U/G-C motif. The magnesium clusters are mainly bound to phosphate groups but also to atoms O6 of G99 (649) G116 (666), G117 (667), G127 (742), to atom O4 of U125 (740) and U128 (743), and to atoms O2 and N3 of C133 (748). The weight of a magnesium cluster coordinated to six water molecules is 120 g/mol, and so it counterbalances the weight of a phosphate group ($PO_4$: 95 g/mol) and thus reduces the flexibility of RNA phosphodiester backbone while screening the phosphate charges. The $Mg^{2+}$ ions

**TABLE 6 Coordination numbers of the $Mg^{2+}$ ions and partner names, with residence times (ns) in parentheses**

| $Mg^{2+}$ ion | Coordination number | Coordination partners |
|---|---|---|
| 144 | 5 | OW-8570(15.0) OW-8572(15.0) OW-8577 (15.0) OW-8584 (15.0) OW-8596 (15.0) |
| 145 | 6 | O2P-112(13.3) OW-4913(15) OW-5012 (15.0) OW-5076 (15.0) OW-5151 (15.0) OW-5551 (15.0) |
| 146 | 6 | O6-107(13.3) O6-135(13.3) OW-8017 (15.0) OW-8035 (15.0) OW-7978 (15.0) OW-8032 (15.0) |
| 147 | 6 | OW-6061(14.9) OW-6063(14.9) OW-6064 (14.9) OW-6171 (14.9) OW-6174 (14.9) OW-8595 (14.9) |
| 148 | 5 | OW-5524(14.4) OW-5568(14.5) OW-5986 (14.6) OW-5992 (14.4) OW-6020 (14.5) |
| 149 | 6 | OW-3038(14.9) OW-3048(14.8) OW-5541 (14.9) OW-5545 (14.8) OW-5564 (14.8) OW-5565 (14.8) |
| 150 | 6 | OW-2368(15.0) OW-3033(15.0) OW-3036 (15.0) OW-3039 (15.0) OW-3045 (15.0) OW-3046 (15.0) |
| 151 | 6 | O1P-107(13.3) OW-5532 (15.0) OW-5543 (15.0) OW-5585 (15.0) OW-5586 (15.0) OW-3101 (14.9) |
| 152 | 6 | O2′-138(13.3) OW-8578 (15.0) OW-8583 (15.0) OW-8585 (15.0) OW-8602 (15.0) OW-9046 (15.0) |

are also bound to the side-chain carboxyl groups of Gln-61 and Asp-73. Over the 48 water molecules bound to $Mg^{2+}$, 23 are bound to fewer than five RNA or protein groups. The ions Mg-147, Mg-148, and Mg-149, which are coordinated only to water molecules, visit the largest number of groups.

The closest neighbors of each $Na^+$ ion were determined for the 11–15-ns interval in s15-rna-mg and s15-rna. Because the coordination partners of the $Na^+$ ions do exchange much faster than those of $Mg^{2+}$ ions, only coordination partners present for more than 0.5 ns are displayed in Table 7. In s15-rna-mg, only 26 such coordination partners are detected for 10 of the 31 $Na^+$ ions present in the simulation. Of these partners, 19 are water oxygens, 4 are base oxygens, and 3 are phosphate oxygens. In s15-rna, 200 coordination partners are observed for 20 of the 49 $Na^+$ ions present in the simulation. The coordination partners are thus more often bound to $Na^+$ ions in the absence of $Mg^{2+}$ ions.

The water bridges between solute chemical groups were analyzed in the 11–15-ns intervals of s15-rna-mg and s15-rna by detecting the water molecules in which the oxygen is a hydrogen bond donor and at least one hydrogen is a hydrogen bond acceptor. The selected hydrogen bonds correspond to distances smaller than 2.0 Å. For each water molecule, the total lifetime of its involvement in bridges was calculated. In s15-rna-mg, 75 water molecules are involved in bridges more than 100 ps, and 4 of them form bridges for more than 1 ns, with lifetimes in the 1.0–2.7 ns range. In s15-rna, 110 water molecules form bridges for more than 100 ps, and 9 bridges have lifetimes larger than 1 ns in the 1.0–4.0 ns range. The more rigid water bridges observed in s15-rna may be a compensating effect for the increased flexibility induced by the $Mg^{2+}$ ion removal.

In contrast, the formation time of each observed bridge and the number of water molecules involved in the bridge are displayed (Supplementary Material) for formation times $>100$ ps. Thirty-three such bridges are observed in s15-rna-mg, whereas 39 are observed in s15-rna. The removal of $Mg^{2+}$ ions greatly increases the number of bridges observed inside S15 in the $\alpha1$-$\alpha2$ loop. The number of bridges observed inside S15 in the $\alpha2$-$\alpha3$ loop decreases, and the bridges observed among His-41, Asp-48, and Ser-51, disappear. The number of bridges between S15 and RNA increase from 9 to 13 when the $Mg^{2+}$ ions are removed. In particular, bridges involving triplets of residues (Gln-61,G140(755),C-141(756)), (Asp-48,G-116(666),U-125(740)), and (Arg-37,His-41, G-126(741)) appear among loop $\alpha2$-$\alpha3$, helix $\alpha3$, and RNA. Four water bridges between S15 and RNA and close to the three-way junction (Thr-21,C-134(749)), (Thr-24,U-136(751)), (Tyr-68,A-138(753)) appear in the absence of $Mg^{2+}$ ions. In s15-rna-mg, inside RNA, two bridges are observed in TL1 and five in the TL2 region, whereas in s15-rna, five bridges are observed in TL1.

## S15-RNA interaction interface

The S15-RNA interaction was analyzed by monitoring, on the 11–15-ns interval, distances chosen in the following way. A set of hydrogen bonds between protein and RNA was first selected by running the program HBPLUS (54) on the initial and final conformations of trajectories s15-rna-mg and s15-rna. Another set of distances was the set of distances quoted in Table 2 of Li et al. (55). Finally, the distances between solute donor and acceptor groups were calculated for each snapshot of s15-rna-mg and s15-rna, and the pairs corresponding to distances smaller than 2.0 Å for more than 100 ps in one trajectory gave the third set of distances analyzed. The total set of atom pairs was analyzed along the trajectories s15-rna-mg and s15-rna by calculating the mean and standard deviation values for the distance hydrogen-acceptor and the angle donor-hydrogen-acceptor. Only the distances displaying a mean value smaller than 3 Å in at least one trajectory are shown in Tables 8 and 9.

Four groups of distances are detected. Group 1 includes distances connecting the helix $\alpha2$ and the G-U/G-C motif, and distances connecting RNA residues inside tetraloop TL2. Group 2 contains distances connecting the helix $\alpha3$ and the three-way junction. Group 3 is a set of distances between the $\alpha1$-$\alpha2$ loop and the three-way junction. Group 4 is formed by intraprotein distances in the $\alpha1$-$\alpha2$ loop. Because the last group of distance is analyzed in the S15-RNA complex as well as in the isolated protein and in structures and MD trajectories, the results are displayed in Table 9.

In group 1 (G-U/G-C motif and TL2), three hydrogen bonds between the residues Arg-34, His-41, and Asp-48 of the protein and G126(741), C124(739), and G117(667) of

**TABLE 7 Coordination partners of the ions $Na^+$ detected more than 500 ps during the 11–15-ns interval of s15-mg-rna and s15-rna**

| $Na^+$ ion | Coordination partners |
|---|---|
| s15-rna-mg | |
| 153 | O6-137 (1.4),OW-2191 (0.6), OW-8836 (0.6), OW-9739 (1.5), OW-11692 (0.6) |
| 156 | OW-3089 (0.7), OW-5937 (0.8), OW-9739 (1.5), OW-10949 (0.5), OW-11171 (0.9) |
| 157 | O2P-104 (0.5), O2P-105 (0.8), OW-3924 (0.7), OW-4219 (0.5), OW-9507 (0.7) |
| 162 | O1P-103 (0.8) |
| 163 | O4-95 (0.7) |
| 165 | O6-137 (1.4), OW-3165 (0.7), OW-3883 (0.7), OW-11171 (0.9) |
| 171 | O6-122 (0.8), OW-8870 (0.5) |
| 175 | OW-3883 (0.7) |
| 178 | OW-10949 (0.5) |
| 179 | OW-8621 (0.5) |
| s15-rna | |
| 153 | OW-1046 (1.0), OW-1579 (0.5), OW-2042 (1.2), OW-2958 (1.5), OW-3304 (1.0), OW-5978 (0.9), OW-6046 (0.6), OW-8032 (1.2), OW-8925 (0.6), OW-9450 (0.8), OW-10607 (0.5), OW-10823 (0.7), OW-11171 (0.5) |
| 155 | OW-884 (0.5), OW-889 (0.7), OW-910 (0.5), OW-1186 (1.2), OW-2958 (1.5), OW-3060 (0.6), OW-4398 (0.8), OW-4419 (0.6), OW-4476 (0.8), OW-5978 (0.9), OW-7116 (1.3), OW-7246 (0.5), OW-7992 (0.6), OW-8344 (0.8), OW-8925 (0.6), OW-9195 (0.6), OW-9427 (0.8), OW-10462 (0.5), OW-10607 (0.5), OW-11171 (0.5), OW-11300 (1.5) |
| 156 | OW-1815 (0.8), OW-1864 (0.7), OW-2000 (1.0), OW-2592 (0.7), OW-2648 (0.6), OW-4526 (0.6), OW-4962 (0.7), OW-5556 (0.8), OW-6984 (0.6), OW-7803 (1.2), OW-8028 (0.6), OW-8032 (1.2), OW-8163 (0.7), OW-9510 (0.7), OW-11031 (0.8), OW-11118 (0.7), OW-11267 (0.6), OW-11374 (0.6) |
| 157 | OW-2000 (1.0), OW-2918 (0.5), OW-3215 (0.9), OW-4715 (0.9), OW-5128 (0.5), OW-7803 (1.2), OW-10025 (0.7) |
| 159 | OW-796 (1.2), OW-1652 (0.6), OW-2452 (0.7), OW-2786 (0.8), OW-5515 (0.8), OW-7327 (1.2), OW-7877 (0.7), OW-11323 (0.6) |
| 163 | OW-1360 (0.8), OW-7862 (1.0), OW-8032 (1.2), OW-8791 (0.6), OW-8913 (1.8), OW-8959 (0.7), OW-9450 (0.8), OW-9479 (0.7) |
| 166 | OW-3234 (0.7), OW-10314 (0.7) |
| 167 | O6-88 (0.7), O6-89 (0.8), OW-1309 (0.6), OW-1369 (0.5), OW-2323 (1.2), OW-5412 (0.6), OW-5589 (1.0), OW-5684 (0.5), OW-6101 (0.8), OW-7821 (0.6), OW-8468 (0.6), OW-8573 (1.9), OW-10307 (0.5), OW-11336 (1.0) |
| 169 | OW-3119 (0.5), OW-8912 (2.5) |
| 170 | O1P-106 (0.5), OW-4913 (0.7), OW-5267 (0.7), OW-5705 (0.9), OW-5786 (3.3), OW-5791 (1.3), OW-7545 (1.1), OW-8785 (0.9), OW-8791 (0.6), OW-8959 (0.7), OW-9365 (1.1), OW-9646 (0.8), OW-9749 (0.7), OW-11340 (0.5) |
| 171 | OW-2323 (1.2), OW-8468 (0.6) |
| 173 | OW-1186 (1.2), OW-1360 (0.8), OW-2042 (1.2), OW-2373 (0.7), OW-3234 (0.7), OW-3667 (1.0), OW-3851 (0.6), OW-4398 (0.8), OW-4476 (0.8), OW-5211 (0.6), OW-5276 (0.7), OW-5978 (0.9), OW-5997 (1.1), OW-7057 (0.5), OW-7125 (0.7), OW-7297 (0.5), OW-7862 (1.0), OW-8032 (1.2), OW-8163 (0.7), OW-8344 (0.8), OW-8913 (1.8), OW-9217 (0.7), OW-9421 (0.5), OW-9479 (0.7), OW-9646 (0.8), OW-9649 (0.5), OW-10530 (1.1), OW-11300 (1.5) |
| 175 | OW-5997 (1.1) |
| 176 | OW-3215 (0.9) |
| 177 | OW-1046 (1.0), OW-1186 (1.2), OW-1865 (1.0), OW-4011 (0.5), OW-8344 (0.8), OW-8913 (1.8), OW-9541 (1.0), OW-10607 (0.5) |
| 179 | OW-7803 (1.2), OW-9559 (1.0), OW-11064 (0.7), OW-11238 (0.6) |
| 180 | OW-1124 (0.7), OW-1624 (0.8), OW-2452 (0.7), OW-3119 (0.5), OW-4108 (1.5), OW-4598 (2.0), OW-6288 (0.6), OW-6858 (0.7), OW-7877 (0.7), OW-8323 (0.6), OW-9291 (0.8), OW-9687 (0.5), OW-10405 (0.5), OW-11323 (0.6) |
| 181 | OW-2373 (0.7), OW-7297 (0.5) |
| 182 | OW-947 (0.6), OW-1186 (1.2), OW-1360 (0.8), OW-1855 (0.9), OW-2544 (0.7), OW-2592 (0.7), OW-2648 (0.6), OW-3215 (1.0), OW-3234 (0.7), OW-3667 (1.0), OW-3851 (0.6), OW-4398 (0.8), OW-5978 (0.9), OW-6046 (0.6), OW-6998 (0.6), OW-7444 (0.7), OW-8028 (0.6), OW-8032 (1.2), OW-8147 (1.2), OW-8785 (0.9), OW-8913 (1.8), OW-9217 (0.7), OW-9510 (0.7), OW-9559 (1.0), OW-5997 (1.1), OW-9649 (0.5), OW-9842 (0.5), OW-10768 (0.6), OW-11267 (0.6), OW-11300 (1.5), OW-11374 (0.6) |
| 183 | OW-6984 (0.6), OW-7821 (0.6) |

The residence times (ns) are in parentheses.

RNA, respectively, are disrupted when the $Mg^{2+}$ ions are removed. These observations are in agreement with the increase of mobility of the complex partners observed near the G-U/G-C motif. On the other hand, Arg-34 forms a transient hydrogen bond with the phosphate group of G107(657), which is located in helix H22 toward the three-way junction. The variations of distances involving residues from helix $\alpha 2$ are in agreement with the decrease of distances between $\alpha 1$ and $\alpha 2$ described earlier. Indeed, if helix $\alpha 2$ reduces its interaction with the G-U/G-C motif, located at one edge of the RNA structure, this helix has a greater possibility of coming closer to $\alpha 1$. In the capping tetraloop TL2, the formation and disruption of hydrogen bonds among U119, U120, C121, G122, and G123 agree with the gap between the phosphate groups of TL2 described above.

Concerning the interaction of the RNA three-way junction with the helix $\alpha 3$ of S15 (group 2), Gln-61, Arg-64, and Arg-71 reinforce hydrogen bonds with G140(755), A138(753), and C139(754) in s15-rna. This observation is consistent with the observation made previously that the helix $\alpha 2$ is reducing its interaction with the G-U/G-C motif (group 1 of distances).

**TABLE 8 Interactions at the atomic level in the S15-RNA complex**

| Atom pair atom1 | res1 | atom2 | res2 | Distance (Å) | Angle (deg) | Formation (%) |
|---|---|---|---|---|---|---|
| s15-rna-mg | | | | | | |
| Group 1 | | | | | | |
| HH12 | Arg-34 | O1P | G107(657) | 6.0 ± 0.5 | 108.4 ± 9.7 | 0.0 |
| HH22 | Arg-34 | O1P | G107(657) | 7.9 ± 0.5 | 107.8 ± 7.5 | 0.0 |
| HH21 | Arg-34 | O1P | G126(741) | 1.9 ± 0.1 | 156.5 ± 10.2 | 96.6 |
| Hδ1 | His-41 | O2′ | C124(739) | 2.0 ± 0.2 | 153.3 ± 12.6 | 85.3 |
| Oδ2 | Asp-48 | H22 | G117(667) | 1.8 ± 0.1 | 166.7 ± 7.2 | 99.2 |
| HO | U119 | O2 | U120 | 3.6 ± 1.9 | 119.3 ± 31.8 | 39.7 |
| O2 | U119 | HO | U120 | 2.6 ± 1.2 | 127.1 ± 54.4 | 67.5 |
| O2P | U119 | H41 | C121 | 2.3 ± 0.5 | 148.3 ± 16.7 | 59.0 |
| O4 | U120 | H22 | G123 | 10.3 ± 1.0 | 144.1 ± 13.0 | 0.0 |
| HO | G122 | O1P | G123 | 2.8 ± 1.1 | 144.2 ± 26.3 | 51.9 |
| Group 2 | | | | | | |
| Hε21 | Gln-61 | O1P | G140(755) | 7.6 ± 0.7 | 39.7 ± 8.5 | 0.0 |
| HH11 | Arg-64 | O2P | G140(755) | 3.6 ± 1.5 | 109.9 ± 49.8 | 36.4 |
| HH | Tyr-68 | O1P | A138(753) | 1.9 ± 0.4 | 156.8 ± 15.5 | 92.5 |
| HH22 | Arg-71 | O3 | A138(753) | 3.9 ± 0.2 | 162.5 ± 10.5 | 0.0 |
| HH12 | Arg-71 | O1P | C139(754) | 2.2 ± 0.5 | 140.9 ± 15.4 | 61.7 |
| HH22 | Arg-71 | O1P | C139(754) | 2.0 ± 0.3 | 149.1 ± 13.5 | 87.2 |
| HH22 | Arg-71 | O5′ | C139(754) | 2.9 ± 0.4 | 130.0 ± 13.0 | 4.7 |
| Group 3 | | | | | | |
| Hζ1 | Lys-7 | O1P | G108(658) | 2.9 ± 0.7 | 77.9 ± 47.1 | 25.4 |
| Hζ2 | Lys-7 | O1P | G108(658) | 2.7 ± 0.7 | 90.8 ± 51.2 | 37.6 |
| Hζ3 | Lys-7 | O1P | G108(658) | 2.8 ± 0.7 | 83.3 ± 46.7 | 29.6 |
| Hζ3 | Lys-7 | O2P | U109(659) | 2.9 ± 0.7 | 79.3 ± 45.8 | 0.0 |
| Oδ2 | Asp-20 | HO2′ | G135(750) | 5.2 ± 0.6 | 105.7 ± 13.3 | 0.2 |
| O | Thr-21 | HO2′ | G107(657) | 1.8 ± 0.1 | 165.1 ± 8.2 | 97.2 |
| Oγ | Thr-21 | H22 | G107(657) | 2.3 ± 0.4 | 141.4 ± 11.5 | 97.2 |
| H | Gly-22 | O2′ | G135(750) | 2.7 ± 0.5 | 138.7 ± 12.0 | 16.8 |
| O | Gly-22 | H22 | G135(750) | 2.2 ± 0.4 | 163.9 ± 8.6 | 70.5 |
| Hε1 | Gln-27 | O2 | C106(656) | 4.0 ± 0.7 | 77.1 ± 11.4 | 0.2 |
| HO | A138(753) | O2P | C139(754) | 3.8 ± 0.3 | 143.5 ± 18.1 | 0.0 |
| s15-rna | | | | | | |
| Group 1 | | | | | | |
| HH12 | Arg-34 | O1P | G107(657) | 2.1 ± 0.7 | 150.2 ± 19.1 | 83.4 |
| HH22 | Arg-34 | O1P | G107(657) | 2.6 ± 1.2 | 137.6 ± 17.6 | 52.8 |
| HH21 | Arg-34 | O1P | G126(741) | 9.7 ± 0.8 | 87.3 ± 14.1 | 0.0 |
| Hδ1 | His-41 | O2′ | C124(739) | 5.3 ± 0.5 | 89.2 ± 14.1 | 0.0 |
| Oδ2 | Asp-48 | H22 | G117(667) | 3.3 ± 0.2 | 141.7 ± 6.3 | 0.0 |
| HO | U119 | O2 | U120 | 2.6 ± 0.5 | 120.8 ± 19.9 | 24.5 |
| O2 | U119 | HO | U120 | 7.1 ± 0.5 | 35.4 ± 22.3 | 0.0 |
| O2P | U119 | H41 | C121 | 8.8 ± 0.6 | 87.6 ± 10.9 | 0.0 |
| O4 | U120 | H22 | G123 | 2.0 ± 0.3 | 156.9 ± 13.7 | 83.6 |
| HO | G122 | O1P | G123 | 3.9 ± 0.3 | 129.5 ± 19.2 | 0.0 |
| Group 2 | | | | | | |
| Hε21 | Gln-61 | O1P | G140(755) | 2.0 ± 0.3 | 155.4 ± 13.1 | 87.5 |
| HH11 | Arg-64 | O2P | G140(755) | 1.8 ± 0.1 | 161.5 ± 8.5 | 99.5 |
| HH | Tyr-68 | O1P | A138(753) | 1.9 ± 0.4 | 161.7 ± 11.3 | 92.3 |
| HH22 | Arg-71 | O3 | A138(753) | 2.0 ± 0.3 | 160.2 ± 12.4 | 85.0 |
| HH12 | Arg-71 | O1P | C139(754) | 1.9 ± 0.3 | 152.8 ± 16.2 | 93.0 |
| HH22 | Arg-71 | O1P | C139(754) | 2.9 ± 0.4 | 123.6 ± 10.8 | 3.2 |
| HH22 | Arg-71 | O5′ | C139(754) | 3.7 ± 0.4 | 135.2 ± 13.9 | 0.0 |
| Group 3 | | | | | | |
| Hζ1 | Lys-7 | O1P | G108(658) | 1.8 ± 0.1 | 158.7 ± 11.3 | 99.2 |
| Hζ2 | Lys-7 | O1P | G108(658) | 3.1 ± 0.2 | 62.5 ± 9.2 | 0.0 |
| Hζ3 | Lys-7 | O1P | G108(658) | 3.3 ± 0.2 | 48.3 ± 7.2 | 0.0 |
| Hζ3 | Lys-7 | O2P | U109(659) | 1.8 ± 0.1 | 159.2 ± 10.3 | 98.7 |
| Oδ2 | Asp-20 | HO2′ | G135(750) | 2.0 ± 0.2 | 145.1 ± 10.4 | 85.5 |
| O | Thr-21 | HO2′ | G107(657) | 2.0 ± 0.2 | 133.8 ± 9.4 | 88.4 |
| Oγ | Thr-21 | H22 | G107(657) | 2.2 ± 0.2 | 143.8 ± 10.6 | 62.2 |

(*Continued*)

**TABLE 8 (*Continued*)**

| Atom pair atom1 | res1 | atom2 | res2 | Distance (Å) | Angle (deg) | Formation (%) |
|---|---|---|---|---|---|---|
| H | Gly-22 | O2′ | G135(750) | 2.4 ± 0.3 | 134.2 ± 13.2 | 23.6 |
| O | Gly-22 | H22 | G135(750) | 2.1 ± 0.2 | 116.4 ± 8.0 | 78.9 |
| Hε1 | Gln-27 | O2 | C106(656) | 2.6 ± 0.5 | 123.5 ± 17.1 | 23.0 |
| HO | A138(753) | O2P | C139(754) | 1.7 ± 0.1 | 158.1 ± 8.8 | 99.3 |

The mean hydrogen-acceptor distances (Å) and the mean donor-hydrogen-acceptor angles (deg) were calculated on the 11–15-ns interval. The formation percentage is the percentage of trajectory time during which the distance is <2.2 Å. The results are compared in s15-rna-mg and in s15-rna.

In the interaction between the $\alpha1$-$\alpha2$ loop and the RNA three-way junction (group 3), the hydrogen bonds between the $NH_3^+$ side-chain group of Lys-7 and the phosphate groups of G108(658) and U109(659) are reinforced in s15-rna. Asp-20 establishes a hydrogen bond with G135(750), as does Gln-27 with C106(656). On the other hand, the hydrogen bond between Thr-21 and G107(657) is less stable in s15-rna. Inside the junction, the residues A138(753) and C139(754) form a hydrogen bond when the $Mg^{2+}$ ions are removed: the formation of this hydrogen bond is facilitated by the absence of $Mg^{2+}$, as A138 is otherwise bound to a magnesium.

From the previous description, one sees that, in the vicinity of the three-way junction, the intermolecular hydrogen bonds between S15 and RNA are mainly strengthened when the $Mg^{2+}$ ions are removed, which is in agreement with the appearance of water bridges between S15 and RNA in that region. Another effect of the $Mg^{2+}$ ion removal is the reorganization of the network of hydrogen bonds involving inside S15, residues located in the loop connecting helices $\alpha1$ and $\alpha2$ (Table 9, part a). Hydrogen bonds are disrupted among residues Arg-16, Asp-20, Thr-21, Gly-22, Thr-24, Glu-25, and Gln-27 and are formed among residues Ser-23, Val-26, and Gln-27. These residues, except Arg-16 and Asp-20, are conserved (56) in S15 proteins from several organisms. This behavior agrees with the water bridges observed among the same group of residues in s15-rna. The N-terminal part of the loop connecting the helices $\alpha1$ and $\alpha2$ is less stable in the absence of $Mg^{2+}$ ions. The MD trajectories s15-rna (Table 9, part a) as well as s15-pdb and s15-aria (Table 9, part b) and the 1ab3 and 2fkx NMR structures of S15 (Table 9, part c) display a similar pattern of formed and nonformed hydrogen bonds, and the isolated S15 proteins (s15-pdb, s15-aria, 1ab3, 2fkx) exhibit a variability of the orientation of $\alpha1$ with respect to the protein core. A similar pattern of hydrogen bonds is observed in the x-ray structure 1a32 (Table 9, part d), where $\alpha1$ protrudes away from the protein core, and in the S15 structures from 2avy and 2aw7 (Table 9, part d), where no high-occupancy site for $Mg^{2+}$ was observed in crystallographic difference density map $F_o - F - c$ (J. Cate, University of California, Berkeley, personal communication, 2006). On the other hand, the hydrogen bond pattern observed in s15-rna-mg is also observed in 1dk1, where the S15-RNA complex is in the presence of $Mg^{2+}$.

## CONCLUSION

The recalculation of the NMR structure of S15, as well as the MD trajectories recorded on the isolated protein, show that the N-terminal helix $\alpha1$ displays different orientations in solution with respect to the protein core. This observation is in agreement with the x-ray structure of the isolated S15 (6), where $\alpha1$ protrudes away from the protein core as a result of intermolecular interactions in the crystal. In the S15-RNA complex, it was proposed (2) that the protein stabilizes the RNA, which is otherwise unfolded. The observations made here on S15 indicate that the protein displays an internal mobility and probably undergoes a conformational drift as well as the RNA during the establishment of the interaction. Measurements of residual dipolar couplings (57) could be used to obtain more precise information on the relative orientations of the $\alpha$-helices inside the protein.

The $Mg^{2+}$ ions form hexacoordinated clusters in the MD trajectory of the S15-RNA complex. Most of these clusters, which interact mainly with the RNA phosphodiester backbone, behave as rigid bodies, which is not very surprising but makes the work presented here consistent with previous observations from MD simulations (19). In the region of the G-U/G-C motif, the removal of $Mg^{2+}$ ions induces an increased mobility of the RNA and of the protein in agreement with the crystal structure in which a $Mg^{2+}$ ion (Mg-150) stabilizes the UUCG tetraloop. On the other hand, in the vicinity of the three-way junction, removal of the $Mg^{2+}$ ions induces the appearance of protein-RNA water bridges and induces reinforcement of several hydrogen bonds between S15 and RNA. The absence of $Mg^{2+}$ ions modifies the network of hydrogen bonds inside the protein loop connecting $\alpha1$ and $\alpha2$. This network then becomes similar to those observed in isolated S15 and in S15-RNA complexes observed in the absence of or in low occupancy of $Mg^{2+}$ ions. Because the $\alpha1$-$\alpha2$ loop is the hinge permitting the mobility of $\alpha1$ with respect to the protein core, the variation of the hydrogen bond network in this loop may play a role in stabilizing the orientation of $\alpha1$ in the S15-RNA complex. The importance of this hydrogen bond network in the S15-RNA complex could be experimentally investigated by mutagenesis. Such an approach has already been used (58) to analyze the importance of residues located in the N-terminal part of the helix $\alpha1$, and the helix was concluded to play no significant role in the

**TABLE 9 Mean values of intraprotein distances (Å) located in the $\alpha$1-$\alpha$2 loop**

(a) s15-rna-mg

| Atom1 | res1 | Atom2 | res2 | Distance (Å) | Angle (deg) | Formation (%) |
|---|---|---|---|---|---|---|
| H | Thr-24 | O | Gly-22 | 2.2 ± 0.2 | 126.4 ± 13.0 | 48.3 |
| H | Thr-24 | Oε1 | Gln-27 | 2.2 ± 0.2 | 132.7 ± 11.1 | 57.2 |
| H | Gly-25 | O | Ser-23 | 2.1 ± 0.3 | 147.2 ± 8.1 | 66.9 |
| H | Arg-16 | Oδ1 | Asp-20 | 1.9 ± 0.2 | 156.6 ± 11.4 | 92.7 |
| H | Gln-27 | O | Ser-23 | 5.5 ± 0.2 | 68.3 ± 3.2 | 0.0 |
| H | Val-26 | O | Ser-23 | 4.3 ± 0.3 | 140.1 ± 7.8 | 0.0 |

s15-rna

| Atom1 | res1 | Atom2 | res2 | Distance (Å) | Angle (deg) | Formation (%) |
|---|---|---|---|---|---|---|
| H | Thr-24 | O | Gly-22 | 4.0 ± 0.2 | 100.2 ± 4.2 | 0.0 |
| H | Thr-24 | Oε1 | Gln-27 | 6.0 ± 0.3 | 42.2 ± 6.3 | 0.0 |
| H | Gly-25 | O | Ser-23 | 3.2 ± 0.2 | 75.6 ± 6.7 | 0.0 |
| H | Arg-16 | Oδ1 | Asp-20 | 4.1 ± 0.3 | 100.8 ± 8.5 | 0.0 |
| H | Gln-27 | O | Ser-23 | 2.3 ± 0.2 | 155.8 ± 11.3 | 40.4 |
| H | Val-26 | O | Ser-23 | 2.4 ± 0.3 | 130.1 ± 14.2 | 31.9 |

(b) s15-pdb

| Atom1 | res1 | Atom2 | res2 | Distance (Å) | Angle (deg) | Formation (%) |
|---|---|---|---|---|---|---|
| H | Thr-24 | O | Gly-22 | 4.0 ± 0.4 | 99.8 ± 6.7 | 0.0 |
| H | Thr-24 | Oε1 | Gln-27 | 9.0 ± 1.0 | 32.0 ± 27.3 | 0.0 |
| H | Gly-25 | O | Ser-23 | 3.2 ± 0.4 | 82.6 ± 10.1 | 0.2 |
| H | Arg-16 | Oδ1 | Asp-20 | 5.7 ± 1.2 | 27.7 ± 23.9 | 0.0 |
| H | Gln-27 | O | Ser-23 | 4.0 ± 0.5 | 140.0 ± 8.7 | 0.1 |
| H | Val-26 | O | Ser-23 | 2.5 ± 0.4 | 158.0 ± 13.0 | 27.1 |

s15-aria

| Atom1 | res1 | Atom2 | res2 | Distance (Å) | Angle (deg) | Formation (%) |
|---|---|---|---|---|---|---|
| H | Thr-24 | O | Gly-22 | 4.1 ± 0.3 | 99.1 ± 4.9 | 0.0 |
| H | Thr-24 | Oε1 | Gln-27 | 6.2 ± 1.1 | 54.2 ± 31.1 | 0.0 |
| H | Gly-25 | O | Ser-23 | 3.3 ± 0.2 | 78.7 ± 8.6 | 0.0 |
| H | Arg-16 | Oδ1 | Asp-20 | 4.1 ± 0.4 | 24.1 ± 5.9 | 0.0 |
| H | Gln-27 | O | Ser-23 | 2.3 ± 0.4 | 150.6 ± 13.4 | 49.4 |
| H | Val-26 | O | Ser-23 | 2.4 ± 0.3 | 123.7 ± 13.2 | 27.8 |

(c) 1ab3

| Atom1 | res1 | Atom2 | res2 | Distance (Å) | Angle (deg) | Formation (%) |
|---|---|---|---|---|---|---|
| H | Thr-24 | O | Gly-22 | 3.9 ± 0.8 | 93.3 ± 15.5 | 0.0 |
| H | Thr-24 | Oε1 | Gln-27 | 7.0 ± 1.5 | 70.6 ± 41.0 | 0.0 |
| H | Gly-25 | O | Ser-23 | 3.6 ± 0.4 | 78.7 ± 6.7 | 0.0 |
| H | Arg-16 | Oδ1 | Asp-20 | 5.1 ± 1.4 | 59.8 ± 27.4 | 5.5 |
| H | Gln-27 | O | Ser-23 | 3.0 ± 0.9 | 142.6 ± 11.2 | 27.8 |
| H | Val-26 | O | Ser-23 | 3.2 ± 0.8 | 116.6 ± 20.5 | 0.0 |

2fkx

| Atom1 | res1 | Atom2 | res2 | Distance (Å) | Angle (deg) | Formation (%) |
|---|---|---|---|---|---|---|
| H | Thr-24 | O | Gly-22 | 3.9 ± 0.8 | 93.4 ± 15.2 | 4.0 |
| H | Thr-24 | Oε1 | Gln-27 | 6.9 ± 1.6 | 73.5 ± 42.3 | 0.0 |
| H | Gly-25 | O | Ser-23 | 3.6 ± 0.4 | 78.7 ± 8.1 | 0.0 |
| H | Arg-16 | Oδ1 | Asp-20 | 5.3 ± 1.4 | 52.7 ± 28.0 | 4.0 |
| H | Gln-27 | O | Ser-23 | 2.9 ± 1.0 | 147.3 ± 13.3 | 28.0 |
| H | Val-26 | O | Ser-23 | 3.2 ± 0.9 | 117.1 ± 17.9 | 0.0 |

| (d) Atom1 | res1 | Atom2 | res2 | 1a32 | 1dk1 | 2avy | 2aw7 |
|---|---|---|---|---|---|---|---|
| N | Thr-24 | O | Gly-22 | 4.1 | 3.3 | 3.3 | 3.5 |
| N | Thr-24 | Oε1 | Gln-27 | 5.9 | 4.0 | 6.7 | 6.7 |
| N | Gly-25 | O | Ser-23 | 3.4 | 2.6 | 3.3 | 3.6 |
| N | Arg-16 | Oδ | Asp-20 | 12.3 | 2.8 | 3.1 | 3.9 |
| N | Gln-27 | O | Ser-23 | 2.9 | 5.4 | 2.8 | 2.9 |
| N | Val-26 | O | Ser-23 | 3.2 | 4.4 | 2.8 | 3.2 |

The mean hydrogen-acceptor distances (Å) and the mean donor-hydrogen-acceptor angles (deg) were calculated on the 11–15-ns interval. The formation percentage is the percentage of trajectory time or of NMR conformers in which the distance is <2.2 Å. The MD trajectories, NMR structures, x-ray structures of isolated S15 (1a32) and of S15-RNA complex (1dk1), and the structures of S15 in two conformations of the ribosome of *E. coli* (2avy and 2aw7) are analyzed. In 1a32 and 1dk1, the atom Oδ1 of Asp-20 is used, whereas in 2avy and 2aw7, the atom Oδ2 of Asp-20 is used.

specific binding of S15 to the rRNA. These results do not contradict our work, as we focus here on residues located in the $\alpha 1$-$\alpha 2$ loop.

## SUPPLEMENTARY MATERIAL

An online supplement to this article can be found by visiting BJ Online at http://www.biophysj.org.

We gratefully thank Dr. Elena Berglund for providing us with the S15 NOE and dihedral restraints files.

The CNRS, University Paris-VII, Institut Pasteur, and grant 11410 from the IDRIS supercomputing center are gratefully acknowledged.

## REFERENCES

1. Recht, M. I., and J. R. Williamson. 2004. RNA tertiary structure and cooperative assembly of a large ribonucleoprotein complex. *J. Mol. Biol.* 344:395–407.
2. Batey, R. T., and J. R. Williamson. 1998. Effects of polyvalent cations on the folding of an rRNA three way junction and binding of ribosomal protein S15. *RNA.* 4:984–997.
3. Nikulin, A., A. Serganov, E. Ennifar, S. Tishchenko, N. Nevskaya, W. Shepard, G. Portier, M. Garber, B. Ehresmann, C. Ehresmann, S. Nikonov, and P. Dumas. 2000. Crystal structure of the S15-rRNA complex. *Nat. Struct. Biol.* 7:273–277.
4. Ennifar, E., A. Nikulin, S. Tishchenko, A. Serganov, N. Nevskaya, M. Garber, B. Ehresmann, C. Ehresmann, S. Nikonov, and O. Dumas. 2000. The crystal structure of UUCG tetraloop. *J. Mol. Biol.* 304: 34–42.
5. Berglund, H., A. Rak, A. Serganov, M. Garber, and T. Härd. 1997. Solution structure of the ribosomal RNA binding protein S15 from Thermus thermophilus. *Nat. Struct. Biol.* 4:20–23.
6. Clemons, W. M., C. Davies, S. W. White, and W. Ramakrishnan. 1998. Conformational variability of the N-terminal helix in the structure of ribosomal protein S15. *Structure.* 6:429–438.
7. Inoue, A., Y. Takagi, and K. Taira. 2003. Importance of magnesium ions in the mechanism of catalysis by a hammerhead ribozyme: strictly linear relationship between the ribozyme activity and the concentration of magnesium ions. *Magnes. Res.* 16:210–217.
8. Walter, F., A. I. Murchie, J. B. Thomson, and D. M. Lilley. 1998. Structure and activity of the hairpin ribozyme in its natural junction conformation: effect of metal ions. *Biochemistry.* 37:14195–14203.
9. Onoa, B., S. Dumont, J. Liphardt, S. B. Smith, I. Tinoco, Jr., and C. Bustamante. 2003. Identifying kinetic barriers to mechanical unfolding of the *T. thermophila* ribozyme. *Science.* 299:1892–1895.
10. Gonzalez, R. L., and I. Tinoco. 1999. Solution structure and thermodynamics of a divalent metal ion binding site in an RNA pseudoknot. *J. Mol. Biol.* 289:1267–1282.
11. Brion, P., and E. Westhof. 1997. Hierarchy and dynamics of RNA folding. *Annu. Rev. Biophys. Biomol. Struct.* 26:113–137.
12. Pitt, S. W., A. Majumdar, A. Serganov, D. J. Patel, and H. M. Al-Hashimi. 2004. Argininamide binding arrests global motions in HIV-1 TAR RNA: comparison with $Mg^{2+}$-induced conformational stabilization. *J. Mol. Biol.* 338:7–16.
13. Al-Hashimi, H. M., S. W. Pitt, A. Majumdar, W. Xu, and D. J. Patel. 2003. $Mg^{2+}$-induced variations in the conformation and dynamics of HIV-1 TAR RNA probed using NMR residual dipolar couplings. *J. Mol. Biol.* 329:867–873.
14. Klein, D. J., P. B. Moore, and T. A. Steitz. 2004. The contribution of metal ions to the structural stability of the large ribosomal subunit. *RNA.* 10:1366–1379.
15. Gerstner, R. B. Y. 2001. Pak, and D.E. Draper. Recognition of 16S rRNA by ribosomal protein s4 from *Bacillus stearothermophilus*. *Biochemistry.* 40:7165–7173.
16. Drygin, D., and R. A. Zimmermann. 2000. Magnesium ions mediate contacts between phosphoryl oxygens at positions 2122 and 2176 of the 23S rRNA and ribosomal protein L1. *RNA.* 6:1714–1726.
17. Kumarevel, T. S., Z. Fujimoto, H. Mizuno, and P. K. Kumar. 2004. Crystallization and preliminary X-ray diffraction studies of the metal-ion-mediated ternary complex of the HutP protein with L-histidine and its cognate RNA. *Biochim. Biophys. Acta.* 1702:125–128.
18. Reblova, K., N. Spackova, J. E. Sponer, J. Koca, and J. Sponer. 2003a. Molecular dynamics simulations of RNA kissing-loop motifs reveal structural dynamics and formation of cation-binding pockets. *Nucleic Acids Res.* 31:6942–6952.
19. Auffinger, P., L. Bielecki, and E. Westhof. 2003. The $Mg^{2+}$ binding sites of the 5S rRNA loop E motif as investigated by molecular dynamics simulations. *Chem. Biol.* 10:551–561.
20. Reblova, K., N. Spackova, J. Koca, N. B. Leontis, and J. E. Sponer. 2003b. Long-residency hydration, cation binding, and dynamics of loop E/helix IV rRNA-L25 protein complex. *Biophys. J.* 87:3397–3412.
21. Gooch, B. D., M. Krishnamurthy, M. Shadid, and P. A. Beal. 2005. Binding of helix-threading peptides to E. coli 16s ribosomal RNA and inhibition of the S15-16s complex. *ChemBioChem.* 6:2247–2254.
22. Culver, G. M., J. H. Cate, G. Z. Yusupova, M. M. Yusupov, and H. F. Noller. 1999. Identification of an RNA-protein bridge spanning the ribosomal subunit interface. *Science.* 285:2133–2135.
23. Bubunenko, M., A. Korepanov, D. L. Court, I. Jagannathan, D. Dickinson, B. R. Chaudhuri, M. B. Garber, and G. M. Culver. 2006. 30s ribosomal subunits can be assembled in vivo without primary binding ribosomal protein S15. *RNA.* 12:1–11.
24. McDowell, S. E., N. Spackova, J. Sponer, and N. G. Walter. 2007. Molecular dynamics simulations of RNA: an in silico single molecule approach. *Biopolymers.* 85:169–184.
25. Gresh, N., J. E. Sponer, N. Spackova, J. Leszczynski, and J. Sponer. 2003. Theoretical study of binding of hydrated Zn(II) and Mg(II) cations to 5-guanosine monophosphate. toward polarizable molecular mechanics for DNA and RNA. *J. Phys. Chem. B.* 107:8669–8681.
26. Dixit, S. B., D. L. Beveridge, D. A. Case, T. E. Cheatham, E. Giudice, F. Lankas, R. Lavery, J. H. Maddocks, R. Osman, H. Sklenar, K. M. Thayer, and P. Varnai. 2005. Molecular dynamics simulations of the 136 unique tetranucleotide sequences of DNA oligonucleotides. ii: sequence context effects on the dynamical structures of the 10 unique dinucleotide steps. *Biophys. J.* 89:3721–3740.
27. Cheatham, T.E., P. Cieplak, and P.A. Kollman. 1999. A modified version of the Cornell et al. force field with improved sugar pucker phases and helical repeat. *J. Biomol. Struct. Dyn.* 16:845–861.
28. Jorgensen, W. L. 1981. Transferable intermolecular potential functions for water, alcohols and ethers. application to liquid water. *J. Am. Chem. Soc.* 103:335–340.
29. Case, D. A., D. A. Pearlman, J. W. Caldwell, T. E. Cheatham III, W. S. Ross, C. L. Simmerling, T. A. Darden, K. M. Merz, R. V. Stanton, A. L. Cheng, J. J. Vincent, M. Crowley, V. Tsui, R. J. Radmer, Y. Duan, J. Pitera, I. Massova, G. L. Seibel, U. C. Singh, P. K. Weiner, and P. A. Kollman. 2002. AMBER 6 and 7. *University of California, San Francisco*, 1999.
30. Darden, T., D. York, and L. Pedersen. 1993. Particule mesh Ewald. *J. Chem. Phys.* 98:10089–10092.
31. Aqvist, J. 1990. Ion-water interaction potentials derived from free energy perturbation simulations. *J. Chem. Phys.* 94:8021–8024.
32. Berendsen, H. J. C., J. P. M. Postma, W. F. van Gunsteren, and A. DiNola. 1984. Molecular dynamics with coupling to an external bath. *J. Chem. Phys.* 81:3684–3690.
33. Ryckaert, J. P., G. Ciccotti, and H. J. C. Berendsen. 1977. Numerical integration of the cartesian equations of motion of a system with constraints: Molecular dynamics of *n*-alkanes. *J. Comput. Phys.* 23: 327–341.

34. Linge, J. P., S. I. O'Donoghue, and M. Nilges. 2001. Automated assignment of ambiguous nuclear Overhauser effects with ARIA. *Methods Enzymol.* 339:71–90.

35. Nederveen, A. J., J. F. Doreleijers, W. Vranken, Z. Miller, C. A. E. M. Spronk, S. B. Nabuurs, P. Guntert, M. Livny, J. L. Markley, M. Nilges, E. L. Ulrich, R. Kaptein, and A. M. J. J. Bonvin. 2005. RECOORD: a REcalculated COORdinates Database of 500+ proteins from the PDB using restraints from the BioMagResBank. *Proteins.* 59:662–672.

36. Linge, J. P., and M. Nilges. 1999. Influence of non-bonded parameters on the quality of NMR structures: A new force field for NMR structure calculation. *J. Biomol. NMR.* 13:51–59.

37. Laskowski, R. A., M. W. MacArthur, D. S. Moss, and J. M. Thornton. 1993. PROCHECK: a program to check the stereochemical quality of protein structure. *J. Appl. Crystallogr.* 26:283–291.

38. Hooft, R. W. W., G. Vriend, C. Sander, and E. E. Abola. 1996. Errors in protein structures. *Nature.* 381:272.

39. Stein, E. G., L. M. Rice, and A. T. Brunger. 1997. Torsion-angle molecular dynamics as a new efficient tool for NMR structure calculation. *J. Magn. Reson.* 124:154–164.

40. Bardiaux, B., T. E. Malliavin, M. Nilges, and A. K. Mazur. 2006. Comparison of different torsion angle approaches for NMR structure determination. *J. Biomol. NMR.* 34:1–15.

41. Linge, J. P., M. A. Williams, C. A. Spronk, A. M. Bonvin, and M. Nilges. 2003. Refinement of protein structures in explicit solvent. *Proteins.* 50:496–506.

42. Schuwirth, B. S., M. A. Borovinskaya, C. W. Hau, W. Zhang, A. Vila-Sanjurjo, J. M. Holton, and J. H. Doudna Cate. 2005. Structures of the bacterial ribosome at 3.5 A resolution. *Science.* 310:827–834.

43. Fan, H., and A. E. Mark. 2003. Relative stability of protein structures determined by x-ray crystallography or NMR spectroscopy: a molecular dynamics simulation study. *Proteins.* 53:111–120.

44. Barthe, P., L. Chiche, N. Declerck, M. A. Delsuc, J. F. Lefevre, T. Malliavin, J. Mispelter, M. H. Stern, J. M. Lhoste, and C. Roumestand. 1999. Refined solution structure and backbone dynamics of $^{15}$N-labeled C12A-p8MTCP1 studied by NMR relaxation. *J. Biomol. NMR.* 15:271–288.

45. Barthe, P., C. Roumestand, H. Demene, and L. Chiche. 2002. Helix motion in protein C12A-p8(MTCP1): comparison of molecular dynamics simulations and multifield NMR relaxation data. *J. Comput. Chem.* 23:1577–1586.

46. Demene, H., T. Ducat, P. Barthe, M. A. Delsuc, and C. Roumestand. 2002. Structure refinement of flexible proteins using dipolar couplings: application to the protein p8MTCP1. *J. Biomol. NMR.* 22:47–56.

47. Murray, L. J. W., W. B. Arendall, D. C. Richardson, and J. S. Richardson. 2003. RNA backbone is rotameric. *Proc. Natl. Acad. Sci. USA.* 100:13904–13909.

48. Miller, J. L., and P. A. Kollman. 1997. Theoretical studies of an exceptionally stable RNA tetraloop: observation of convergence from an incorrect NMR structure to the correct one using unrestrained molecular dynamics. *J. Mol. Biol.* 270:436–450.

49. Simmerling, C., J. L. Miller, and P. Kollman. 1998. Combined locally enhanced sampling and particle mesh ewald as a strategy to locate the experimental structure of a non-helical nucleic acid. *J. Am. Chem. Soc.* 120:7149–7155.

50. Cheong, C., G. Varani, and I. Tinoco, Jr. 1990. Solution structure of an unusually stable RNA hairpin, 5'GGAC(UUCG)GUCC. *Nature.* 346: 613–614.

51. Allain, F. H., and G. Varani. 1995. Structure of the P1 helix from group I self-splicing introns. *J. Mol. Biol.* 250:333–353.

52. Tishchenko, S., A. Nikulin, N. Fomenkova, N. Nevskaya, O. Nikonov, P. Dumas, H. Moine, B. Ehresmann, C. Ehresmann, W. Piendl, V. Lamzin, M. Garber, and S. Nikonov. 2001. Detailed analysis of RNA-protein interactions within the ribosomal protein S8-rRNA complex from the archaeon *Methanococcus jannaschii*. *J. Mol. Biol.* 311: 311–324.

53. Auffinger, P., L. Bielecki, and E. Westhof. 2004. Symmetric $K^+$ and $Mg^{2+}$ ion-binding sites in the 5S rRNA loop E inferred from molecular dynamics simulations. *J. Mol. Biol.* 335:555–571.

54. McDonald, I. K., and J. M. Thornton. 2003. Satisfying hydrogen bonding potential in proteins. *J. Mol. Biol.* 238:777–793.

55. Li, W., B. Ma, and B. A. Shapiro. 2003. Binding interactions between the core central domain of 16S rRNA and the ribosomal protein S15 determined by molecular dynamics simulations. *Nucleic Acids Res.* 31: 629–638.

56. Serganov, A., L. Benard, C. Portier, E. Ennifar, M. Garber, B. Ehresmann, and C. Ehresmann. 2001. Role of conserved nucleotides in building the 16s rRNA binding site for ribosomal protein S15. *J. Mol. Biol.* 305:785–803.

57. de Alba, E., and N. Tjandra. 2004. Residual dipolar couplings in protein structure determination. *Methods Mol. Biol.* 278:89–106.

58. Revtovich, S. W., A. D. Nikulin, and S. V. Nikonov. 2004. Role of N-terminal helix in interaction of ribosomal protein S15 with 16S rRNA. *Biochemistry (Mosc.).* 69:1319–1323.

59. Leontis, N. B., and E. Westhof. 2003. Analysis of RNA motifs. *Curr. Opin. Struct. Biol.* 13:300–308.

60. Jossinet, F., and E. Westhof. 2005. Sequence to structure (s2s): display, manipulate and interconnect RNA data from sequence to structure. *Bioinformatics.* 21:3320–3321.

61. DeLano, W. L. 2002. The PyMOL Molecular Graphics System. *http://www.pymol.org*.